Variability of ETAS parameters in global subduction zones and applications to mainshock-aftershock hazard assessment

Lizhong Zhang[1,2], Maximilian J. Werner[2], and Katsuichiro Goda[1,3]

[1]Department of Civil Engineering, University of Bristol, Queen's Building, Bristol BS8 1TR, United Kingdom

[2]School of Earth Sciences and Cabot Institute, University of Bristol, Wills Memorial Building Queens Road, Bristol BS8 1RJ, United Kingdom

[3]Department of Earth Sciences, University of Western Ontario, Biological and Geological Sciences Building, 1151 Richmond Street North, London, Ontario N6A 5B7, Canada

Corresponding Author: Lizhong Zhang

Corresponding Author E-mail: lz0560@my.bristol.ac.uk

Online Material: Coordinates of spatial windows for ETAS parameter estimation, residual analysis of Cases 1 and 2, and log-likelihood values and Akaike Information Criterion values for Cases 1 and 2.

Abstract

Megathrust earthquake sequences can impact buildings and infrastructure due to not only the mainshock but also the triggered aftershocks along the subduction interface and in the overriding crust. To give realistic ranges of aftershock simulations in regions with limited data and to provide time-dependent seismic hazard information right after a future giant shock, we assess the variability of the ETAS model parameters in subduction zones that have experienced **M**≥7.5 earthquakes, comparing estimates from long time windows with those from individual sequences. Our results show that the ETAS parameters are more robust if estimated from a long catalog than from individual sequences, given individual sequences have fewer data including missing early aftershocks. Considering known biases of the parameters (due to model formulation, the isotropic spatial aftershock distribution, and finite size effects of catalogs), we conclude that the variability of the ETAS parameters that we observe from robust estimates is not significant, neither across different subduction zone regions nor as a function of maximum observed magnitudes. We also find that ETAS parameters do not change when multiple **M**8.0-**M**9.0 events are included in a region, mainly because a **M**9.0 sequence dominates the number of events in the catalog. Based on the ETAS parameter estimates in the long time period window, we propose a set of ETAS parameters for future **M**9.0 sequences for aftershock hazard assessment (K_0 = 0.04±0.02, α = 2.3, c = 0.03±0.01, p = 1.21±0.08, γ =1.61±0.29, d = 23.48±18.17, and q = 1.68±0.55). Synthetic catalogs created with the suggested ETAS parameters show good agreement with three observed **M**9.0 sequences since 1965 (the 2004 **M**9.1 Aceh-Andaman earthquake, the 2010 **M**8.8 Maule earthquake, and the 2011 **M**9.0 Tohoku earthquake).

Introduction

Megathrust subduction earthquakes trigger numerous aftershocks over a prolonged period of time and a range of distances. The seismicity rate increases significantly and then decays in time, sometimes punctuated by secondary aftershock sequences. Large aftershocks have been triggered at distances of more than 100 km and may occur months later (Toda *et al.*, 2011). Over eighty **M**≥5.5 aftershocks were triggered within two months of the 2004 **M**9.1 Aceh-Andaman earthquake, while the 2011 **M**9.0 Tohoku earthquake triggered circa 200 M_j≥5.5 aftershocks within two months, according to the National Earthquake Information Center (NEIC) and Japan Meteorological Agency (JMA) catalogs, respectively. The aftershocks are triggered not only near the subduction interface but also in the upper crust of onshore regions. Shallow aftershocks near population centers and critical infrastructures can be particularly dangerous. For instance, the Maule, Chile earthquake on 27 February 2010 triggered shallow onshore **M**6.9 and **M**7.0 earthquakes on 11 March about 200 km from the mainshock near Pichilemu. These two triggered events occurred within 15 minutes and 11 km of each other (Farías *et al.*, 2011; Ryder *et al.*, 2012). A month after the Tohoku mainshock, the Yunodake and Itozawa faults ruptured, and a large aftershock of **M**6.6 struck near the Fukushima Nuclear Power Plant 240 km from the epicenter of the Tohoku mainshock (Fukushima *et al.*, 2013; Toda and Tsutsumi, 2013). For effective earthquake risk management, the increased aftershock rates in space and time along the subduction plate interface and in the shallow onshore crust should be considered (Ebrahimian *et al.*, 2014; Iervolino *et al.*, 2015; Field *et al.*, 2017; Zhang *et al.*, 2018).

To assess the effect of aftershocks triggered by megathrust subduction earthquakes on seismic hazard and risk analysis, Zhang *et al.* (2018) developed a new simulation framework for spatiotemporal seismic hazard and risk assessment of **M**9.0 earthquake sequences. They built a new spatially anisotropic aftershock kernel and combined a simulated 2D mainshock rupture plane from a rupture scaling law (e.g., Thingbaijam *et al.* (2017)) with a power law beyond the rupture in the Epidemic Type Aftershock Sequence (ETAS) simulation. A case study of the 2011 Tohoku sequence showed that synthetic catalogs compared well with observations. To provide seismic hazard and risk information in other subduction zones, however, we need to assess the variability of ETAS model parameters in different subduction zones. This is particularly important for the regions where major earthquakes are anticipated in the future but few or none have been observed, such as in the Mentawai subduction zone in Indonesia (Natawidjaja *et al.*, 2006) and the Cascadia subduction zone in North America (Wang and Tréhu, 2016).

Given a sufficiently complete and long earthquake catalog, one might expect the variability of ETAS parameters is insignificant across different subduction-zone regions. The ETAS model synthesizes different empirical 'laws' of seismicity, including the Gutenberg-Richter law, the Omori-Utsu law, and the Utsu-Seki law, which are universally observed and appear robust. A single set of the ETAS parameters might be sufficient for forecasting spatiotemporal earthquake sequences in subduction zones globally for hazard purposes.

Prior research has mostly focused on ETAS parameter variations in different tectonic settings. Chu *et al.* (2011) found that the ETAS parameters vary across different tectonic settings, but interpreted these differences as a result solely of different absolute seismicity rates rather than necessary differences in clustering properties across zones. Similarly, Page *et al.* (2016) investigated the spatial variation of the aftershock productivity in different tectonic regions and concluded that the variability of aftershock productivity in the same tectonic region is less than the variability across different tectonic regions. Utsu *et al.* (1995) reviewed p-value variations with tectonic conditions, including stress, heat flow, temperature, etc. Heat flow appears broadly stable across different subduction zones (Zaliapin and Ben-Zion, 2016), so the p-values might also be stable. Narteau *et al.* (2009) found that the c-value in Omori's law depends on fault type and possibly differential stress, indicating that thrust events have smaller *c*-values than normal and strike-slip events. On the other hand, some studies that focused on individual sequences suggested a regional dependence of the Gutenberg-Richter law and the Omori-Utsu law (Utsu *et al.*, 1995; Shcherbakov *et al.*, 2013; Wetzler *et al.*, 2016). Substantial variations of the ETAS parameters have been reported in different regions from sequence to sequence (e.g., Kumazawa *et al.*, 2014; Nicolis *et al.*, 2015; Zakharova *et al.*, 2017). Currently, whether ETAS parameters vary significantly in time or space in subduction zones remains unclear.

Past studies used different versions of the ETAS models calibrated to different catalogs (e.g., global (Chu *et al.*, 2011; Bansal and Ogata, 2013) or local (Nicolis *et al.*, 2015)) to characterize the occurrence and triggering of earthquakes in subduction zones. Because of differences of the catalogs' quality and spatiotemporal data windows, the magnitude completeness (M_c) significantly differs across regions. Sornette and Werner (2005a) argued that ETAS parameters change with completeness magnitude, implying that parameter comparisons should be made at the same completeness magnitude. In addition, different formulations of ETAS models can lead to different ETAS parameters. Therefore, it is difficult to compare ETAS parameters from the literature. For example, Chu *et al.* (2011) estimated ETAS parameters from the NEIC catalog with cut-off magnitude (M_{cut}) =5.0 in different tectonic zones. Bansal and Ogata (2013) applied the ETAS model using the NEIC catalog with M_{cut}=4.7 to assess the change of seismicity rates before the 2004 Aceh-Andaman earthquake. Nicolis *et al.* (2015) investigated the change of seismicity rates in Chile from 2007 to 2014 using the local Chilean catalog with M_{cut}=3.0, during which two major subduction earthquake sequences occurred (i.e., the 2010 Maule and 2014 Iquique earthquakes). To have a fair comparison and investigate the change of the ETAS parameters in different subduction-zone regions, the sub-catalog for the parameter estimation should be processed in a consistent way across different regions.

This study assesses patterns of the ETAS parameters by focusing on zones that experienced subduction-zone **M**≥7.5 earthquakes. We investigate whether ETAS parameters depend on the magnitudes and/or locations of the largest earthquakes. In addition, some megathrust events occurred nearby within the same subduction zone (e.g., the 2010 Maule and 2015 Illapel earthquakes), providing an opportunity to investigate the effect of multiple megathrust subduction earthquakes in the same subduction zone on the ETAS parameters. After examining the variability of the ETAS parameters, we propose a representative set of global **M**9.0 subduction-zone ETAS parameters for the purpose of mainshock-aftershock sequence hazard and risk assessments. The parameter choices take into account known parameter biases resulting from the assumption of isotropic distributions of aftershocks in the ETAS parameter estimation.

The objectives of this study are three-fold:

(1) To assess the variability of earthquake clustering statistics across subduction zones, characterized in terms of productivity, temporal, and spatial parameters of the ETAS model.

(2) To evaluate the effect of multiple subduction earthquake sequences on the variability of the ETAS parameters by focusing on regions where multiple large (**M**≥8.3) events occurred recently (e.g., Western Indonesia, Chile, and Eastern Japan).

(3) To develop a global **M**9-class ETAS simulation framework. We demonstrate its applicability by comparing observed and synthetic aftershocks of the 2004 Aceh-Andaman earthquake, the 2010 Maule earthquake, and the 2011 Tohoku earthquake.

ETAS Model

In this section, we present the standard ETAS model formulation for parameter estimation, following Zhuang *et al.* (2002) and Seif *et al.* (2017). The total seismic rate $\lambda(t, x, y|H_t)$ of the ETAS model at time t and location (x, y) includes a background rate $\mu(x,y)$ and a triggering rate $g(t - t_j, x - x_j, y - y_j; M_j)$:

$$\lambda(t, x, y|H_t) = \mu(x, y) + \sum_{j:t_j<t} g(t - t_j, x - x_j, y - y_j; M_j) \tag{1}$$

where H_t is the observed seismicity up to time t ($H_t = \{x_j, y_j, t_j, M_j\}; t_j<t$). The triggering function $g(t,x,y;M)$ consists of the productivity ($K_0\ e^{\alpha(M-M_{cut})}$), the normalized Omori-Utsu function $v(t)$, and a spatial distribution $f(x,y|M)$ of triggered events:

$$g(t, x, y; M) = K_0\ e^{\alpha(M-M_{cut})}\ v(t)\ f(x, y|M) \tag{2}$$

where M_{cut} is the cut-off magnitude to select earthquakes larger than M_{cut}. K_0 (events/day) and α are the productivity parameters. K_0 measures the intensity of aftershock generation, defining the number of triggered events above M_{cut}, whereas α determines how the triggering productivity of an earthquake increases with magnitude.

The temporal function is the normalized Omori-Utsu law:

$$v(t) = c^{p-1}(t + c)^{-p}(p - 1) \tag{3}$$

where c (days) and p are parameters. c is applied to eliminate a singularity at $t = 0$. The p-value is associated with the decay rate of aftershocks in time.

The spatial distribution of triggered events is defined by:

$$f(x, y|M) = \frac{(q-1)}{\pi\left(x^2+y^2+d\ e^{\gamma(M-M_{cut})}\right)}\left(1 + \frac{x^2+y^2}{d\ e^{\gamma(M-M_{cut})}}\right)^{-q} \tag{4}$$

where d (km^2), q, and γ are parameters. $d\ e^{\gamma(M-M_{cut})}$ is a measure of the source dimension and scales the spatial aftershock footprint, whereas q describes the spatial decay of aftershocks.

ETAS Parameter Estimation and Stochastic Declustering

The ETAS parameters are obtained via the maximum likelihood estimation (MLE) (Seif *et al.*, 2017). The log-likelihood function can be expressed as follows:

$$logL = \sum_{i=1}^{n} \log\left(\lambda\left(t_i, x_i, y_i \middle| H_{t_i}\right)\right) - \int_S \int_0^T \lambda(t, x, y)dt\, dx\, dy \quad (5)$$

where n is the number of events in the target window, λ is the total seismic rate from Equation (1), and S and T are the spatial and temporal ranges of the target window. Since the ETAS model (Equation (1)) divides the input seismicity into background and triggered events, we used the same algorithm as Zhuang *et al.* (2002), who developed stochastic declustering for the ETAS parameter estimation. Therefore, rather than declustering the catalog before the parameter estimation, the spatial background rate is estimated jointly, and the probability of background event (φ_i) is calculated by:

$$\varphi_i = \frac{\mu(x_i, y_i)}{\lambda(x_i y_i t_i)} \quad (6)$$

where φ_i is the probability that the event$_i$ is a background event. $\mu(x_i, y_i)$ and $\lambda(x_i y_i t_i | H_{t_i})$ are the background rate and the total seismicity rate, respectively, in Equation (1). The background rate is estimated with adaptive Gaussian kernels (Zhuang *et al.*, 2002). We refer the reader to Zhuang *et al.* (2002) for a detailed explanation.

To estimate the parameters of the ETAS model reliably, the input earthquake catalog needs to be complete and homogeneous over an appropriate target window. The target window specifies a range of space, time, and magnitude to filter seismic events. However, some events outside the target window may trigger seismic events in the target window. Therefore, an auxiliary window is often introduced to reduce the bias (Wang *et al.*, 2010). To process the data consistently, the following procedure is implemented to identify the spatial auxiliary and target windows:

1. The spatial target window is considered as the rupture area of the subduction mainshock with a 50% extension on each side, i.e. the spatial target window is twice as large as the rupture length and width, as suggested by Kagan (2004).
2. The spatial auxiliary window is 30% larger than the spatial target window on each side.
3. Events with depths less than 100 km are considered.

The relatively large spatial windows that are twice as large as the rupture length suggested by Kagan (2002, 2004), partially as a result of the large location errors in global catalogs (Kagan, 2004). The spatial selection approach by Kagan (2002) was also tested and used by others (Shcherbakov *et al.*, 2004; Nanjo *et al.*, 2007). Since the rupture models of recent megathrust events are available (Mai and Thingbaijam, 2014), the rupture dimensions are taken from the rupture models rather than the scaling law of Kagan (2002).

Table 1 summarizes three cases of temporal windows to investigate the triggering characteristics in subduction zones of a variety of sequences of different magnitudes estimated over (1) long time periods and (2) short time periods (individual sequences):

- Case 1: To investigate whether ETAS parameters vary systematically across regions or with maximum magnitudes in a region, we use a long temporal window between 1981 and 2017, of which the first five years are considered as the auxiliary window.
- Case 2: Because the poor assumption of an isotropic spatial aftershock distribution in Equation (4) is known to bias K_0 and α (Hainzl *et al.*, 2013), we fix α=2.3 in Case 2 and re-estimate parameters, following Seif *et al.* (2017). The same sub-catalogs are used as in Case 1.
- Case 3: To assess whether ETAS parameters vary among individual sequences, we estimate parameters over shorter time periods that increase with the magnitude of the largest earthquake. For mainshocks with 7.5≤**M**<8.0, the temporal auxiliary and target windows are set to 0.5 and 1 year, respectively. For 8.1≤**M**<8.7, the temporal auxiliary

and target windows are 1 and 2 years, respectively, whereas for **M**≥8.7 the temporal auxiliary and target windows are 2 and 4 years, respectively. These target windows of 1, 2, and 4 years cover 91%, 93%, and 94% of the total rate for a single generation of triggered events, respectively, assuming a typical Omori law with $p = 1.28$ and $c = 0.05$ (Zhang *et al.*, 2018).

ETAS Residual Analysis

Residual analysis (Ogata, 1988; Werner, 2007; Harte, 2012; Kumazawa *et al.*, 2014; Lombardi, 2017a) is a useful tool for checking the goodness-of-fit of the ETAS model to an earthquake catalog. A transformed time sequence τ_i is calculated as:

$$\tau_i = \int_S \int_0^{t_i} \lambda(t, x, y) dt\, dx\, dy \quad (7)$$

which is the integral of the conditional intensity function (λ) from 0 to t_i (time of the ith event in Equation (5)) in the region *S*. The transformed time follows a stationary Poisson process with unit rate if the ETAS model fits the catalog well (Ogata, 1988). The goodness-of-fit assessment is based on the expectation that a well calibrated conditional intensity function should integrate to the observed number of events, i.e. the integral of λ to the ith event should equal i (within fluctuations of a Poisson process). Significant deviations from the unit rate beyond the expected randomness of a unit-rate Poisson process indicate that either too few or too many events are occurring with respect to the model's anticipated rate. We use residual analysis as a visual quality check to gauge the model fit, noting however that our purpose is the stochastic simulation of aftershocks and its application to hazard, rather than strict hypothesis testing.

Data

Earthquake Catalogs of Global M≥7.5 Subduction Earthquakes

To compare the ETAS parameters from different regions in a consistent way, the NEIC catalog (see Data and Resources) is used for all parameter estimations. The NEIC has been used in several global studies of aftershock statistics (e.g. Kagan, 2004; Shcherbakov *et al.*, 2013; Page *et al.*, 2016). We select the time period from 1981 to 2017 for model calibration (**Table 1**). In response to improved detection capability, the IASPEI Seismic Format was introduced to the NEIC catalog in January 1999 (Storchak *et al.*, 2003) and we therefore select global megathrust subduction earthquakes from 1999 to 2017 to obtain reasonably complete sub-catalogs of aftershocks. These are summarized in **Table 2** together with source information from Hayes *et al.* (2017). The majority of events listed in **Table 2** are thrust subduction events with dip angles of less than 30º. The global subduction catalogs also include oblique reverse events with considerable components of thrust that occurred on plate boundaries (Events 23, 26, and 28 in Western Indonesia, Philippines, and North America, respectively) (Ye *et al.*, 2012; Kao *et al.*, 2015). In particular, we included Event 28 (the 2012 **M**7.8 Haida Gwaii event) in Western Canada, which Hyndman (2015) concluded to be a megathrust event and is the largest thrust event ever recorded near the North Cascadia subduction zone (Bird and Lamontagne, 2015). The index number of each event is shown in the first column of **Table 2**. Mainshock rupture models are adopted from the SRCMOD database (Mai and Thingbaijam, 2014) (see Data and Resources). Because rupture models of some **M**7.5-8.0 earthquakes are not available in SRCMOD, these are collected from the U.S. Geological Survey (USGS) (see Data and Resources). **Table 2** also lists the effective length and width of each slip model which we calculated using autocorrelation widths following Thingbaijam and Mai (2016). **Figure 1** shows the locations of the megathrust events classified by regions.

To ensure that ETAS parameter variations do not simply reflect differences in the quality of a catalog, the sub-catalogs need to be homogeneous. The results of M_c and *b*-value estimation (Shi and Bolt, 1982; Marzocchi and Sandri, 2003; Woessner and Wiemer, 2005), and the number of events **M**≥4.5 for Cases 1 and 2 (**Table 1**) are shown in **Table 2**. To ensure that parameter estimates are reliable and comparable, the sub-catalogs with higher bulk completeness threshold M_c>4.5 and those with less than 100 events above **M**4.5 are excluded. This leaves 21, 21, and 16 sub-catalogs for Cases 1, 2, and 3, respectively. The coordinates of spatial auxiliary and target windows are provided in the electronic supplement (see **Table S1** available in the electronic supplements to this article). Some space-time volumes in **Table 2** do not have a sufficient number of events, because their numbers vary with target window size (scaled by the largest earthquake size), aftershock productivity, background rate, missing early aftershocks, and possibly offshore completeness variations.

The effective rupture length and width of each event in **Table 2** are compared with the length-width scaling relationships by Thingbaijam *et al.* (2017) in **Appendix A**. We will use this scaling law (and its prescribed uncertainty) to simulate variability of the anisotropic mainshock rupture dimension in the **ETAS Simulations of M9-class Events section**. The observation from **Appendix A** suggests that the scaling law from Thingbaijam *et al.* (2017) can be used to simulate the mainshock rupture planes of **M**8.0-9.0 events in the ETAS simulation framework, and that predicted widths/lengths of **M**7.5-**M**7.9 earthquakes might need a slightly larger standard deviation to capture the observed variability.

Comparison of ETAS Parameters by Region and Magnitude

This section discusses the productivity parameters (K_0 and α), temporal parameters (c and p), and spatial parameters (γ, d and q) of the ETAS model and their variability within global subduction regions. All ETAS parameters are classified according to regions and the largest magnitudes to investigate any systematic changes for Cases 1-3 shown in **Table 1** (Case 1: longer catalogs with free α, Case 2: longer catalogs with fixed α, and Case 3: individual sequences with free α). Regional classification is solely based on geographical proximity, which is shown in **Figure 1**. To show robust estimates from different cases, we only present the ETAS parameter results with $q < 4$ and $d < 500$ from Cases 1-3. Unusually large q and d values indicate insufficient data with distance to fit the spatial power law robustly (Seif *et al.*, 2017). This leads to 18, 18, and 10 parameter sets for Cases 1, 2, and 3, respectively.

In the following, we first present the ETAS parameter results of Case 1 based on long-time catalogs. To dismiss the bias of the isotropic spatial distribution to the productivity parameters, Case 2 re-estimates the ETAS parameters using the same catalogs as Case 1 with fixed α. The residual analysis of Cases 1 and 2 is also compared. The ETAS parameters from Case 3 are estimated based on the temporal target windows of individual sequences as defined in **Table 1**.

In each case, we compare the estimated ETAS parameters with the literature and explain possible reasons for bias in the ETAS parameters. To compare the ETAS parameters quantitatively, we calculate the median ETAS parameters and their standard errors across different regions. We also quantify the dependence of the ETAS parameters on the largest magnitude and rupture dimensions using a test of correlation (e.g., Luco *et al.*, 2002). At the end of each subsection, we quantify the variability of the ETAS parameters of each case to infer the robustness of the estimate values.

Case 1 - Long Time Period Catalogs

Regional Dependence of ETAS Parameters in Case 1

Figure 2 shows the ETAS parameter results of Case 1 classified by region. From previous studies, we expect K_0 and α values to lie in the range 0.006-0.8 and 1.1-2.3, respectively (Ogata and Zhuang, 2006; Seif *et al.*, 2017; Zhang *et al.*, 2018). Several lines of credible evidence advocate that α should equal 2.3, which corresponds to $\alpha = b \ln 10$ with b=1.0 (Helmstetter *et al.*, 2005, 2006; Hainzl *et al.*, 2008; Seif *et al.*, 2017). We observe, however, a broad range of K_0 and α values, which we ascribe to two known effects. First, these two productivity parameters are anti-correlated, because of the mathematical formulation of the model (Sornette and Werner, 2005b; Lombardi, 2017b). Second, since the modeled spatial aftershock distribution is isotropic, while observed aftershocks distribute anisotropically, α is underestimated and K_0 is overestimated (Hainzl *et al.*, 2008; Seif *et al.*, 2017). An example of this bias arises for Event 10 (the **M**9.1 2004 Aceh-Andaman earthquake), whose rupture length (970 km) is much larger than its rupture width (200 km) (see **Table 2** and **Figure 1A**(a) and (b)), while its α value is the smallest of all sub-catalogs and its K_0 is the second highest.

To further investigate the relationship between the productivity parameters and the anisotropy of large earthquake sequences, **Figure 3** shows a plot of α against K_0. An inverse relationship between α and K_0 can be observed in **Figure 3**, as expected from Sornette and Werner (2005b). The ratio of the effective rupture length and width of the mainshock is color-coded for each sub-catalog. A large length-to-width (L/W) ratio indicates the anisotropy of aftershock sequences, which could bias the productivity parameters (Hainzl *et al.*, 2008). For example, in **Figure 3** four out of five sub-catalogs have K_0 values larger than 0.3 and moderate to large L/W ratios (L/W ratios>2.5) including all **M**9.0 class events. Except for Event 20 (the 2009 New Zealand earthquake), all the events with L/W ratios<1.5 have K_0 values less than 0.3. We further looked at the sub-catalog of Event 20 in New Zealand. Multiple **M**7.0 thrust events were recorded in the South Island of New Zealand including the 1993 **M**7.0 and 2003 **M**7.2 events, which might have an impact on the ETAS parameter estimation of Event 20. To reduce the bias due to the isotropic model, α will be fixed in Case 2 based on long-time catalogs and further discussion will be given in **Case 2 - Long Time Period Catalogs with Fixed α section**.

Typical ranges of *p* and *c*-values from the long-time catalog for the Tohoku region are 1.05-1.16 and 0.0215-0.0245, respectively (Ogata and Zhuang, 2006; Zhang *et al.*, 2018). These temporal parameters are also known to be subject to potential bias due to a small sample size of early aftershocks in the sub-catalog that leads to a large *c*-value (Hainzl, 2016; Seif *et al.*, 2017). The four largest *c*-values with greater uncertainties shown in **Figure 2**(c) correspond to Events 5, 9, 16 and 20 with relatively small numbers of events (322, 329, 509, and 269) in Philippines, Indonesia, Peru, and New Zealand, respectively. This highlights the difficulty to estimate *c* with a smaller number of events. In **Figure 2**(c) and (d), the *c*- and *p*-values of **M**9-class Events 10, 21, and 25 are robust and consistent with those found by Zhang *et al.* (2018). The small to moderate variations of the temporal parameters appear consistent with under-sampling and missing early aftershocks in the sub-catalogs of the **M**7.5-8.5 events.

Typical ranges of spatial parameters from recent studies (e.g., Ogata and Zhuang, 2006; Seif *et al.*, 2017; Zhang *et al.*, 2018) are *d* = 7.89-29.92, *γ* = 1.32-1.69, and *q* = 1.59-2.13. *γ* and *d* define the scaling of spatial aftershock distributions with mainshock magnitude. A large *γ* value (e.g., *γ* > 1.5) reflects a better fit to the isotropic power law of the ETAS model. Assuming constant stress drop for different earthquakes, several studies argued γ should equal ln(10) = 2.3, such that ruptures scale according to $e^{0.5\log(10)\cdot M}$ (Helmstetter *et al.*, 2005; Seif *et al.*, 2017). Similarly to K_0 and α in the productivity term, γ and *d* values are also anti-correlated due to the mathematical formulation of the isotropic spatial distribution. *q* describes the aftershock decay in the far field. A large *q* indicates a fast decay due to the limited number of events outside the mainshock rupture plane (Seif *et al.*, 2017). In **Figure 2**(e), *d*-values are larger than the observed ranges (7.89-29.92) from the literature. On the other hand, the *γ* values are systematically lower than expected in **Figure 2**(f), only Events 10, 18, and 21 in Indonesia and

Chile have γ values greater than 1. This can be explained by a lack of aftershocks, resulting in overestimated d and underestimated γ-values (Seif *et al.*, 2017). The q-values range between 1.6-2.4 in **Figure 2**(g). Considering the uncertainty this is consistent with results by Ogata and Zhuang (2006) and Zhang *et al.* (2018).

To quantify the change of the ETAS parameters across regions, boxplots of the ETAS parameters in each region and the detailed calculation of the total standard error of each parameter for the boxplots are provided in **Appendix B**. Due to a small number of sub-catalogs in North America, Japan, Eastern Indonesia, Western Indonesia, and New Zealand, the variability of the parameters in these regions might be affected by the number of events associated with the maximum magnitude. The differences between the maximum observed magnitudes (7.5≤**M**≤9.0) and M_{cut} lead to significantly different numbers of events in the target windows. We therefore focus on the boxplots of Papua New Guinea (8 sub-catalogs with **M** from 7.7 to 8.8) and South America (4 sub-catalogs with **M** from 7.5-8.1) given their larger number of sub-catalogs and wider magnitude ranges. Considering the medians and interquartile ranges, we see little evidence for systematic parameter differences between Papua New Guinea and South America. We interpret individual parameter variations as due to different largest magnitudes in the same region and the known biases due to the model formulation. In summary, we do not observe a clear dependence of ETAS parameters on regions in Case 1.

Magnitude Dependence of ETAS Parameters in Case 1

To assess the dependence of the ETAS parameters on the magnitudes of the largest earthquakes within the sub-catalogs, the estimated parameters of Case 1 are grouped by the largest magnitudes in **Appendix B**. We observe that, except for the productivity parameters which are biased by the model formulation and anisotropy of aftershocks, temporal and spatial parameters of **M**9.0 events are robust across different subduction zones with small standard errors. The parameters of sub-catalogs of **M**7.5-8.5 events vary more than those of **M**9.0 events with greater errors.

To quantify the dependence of the ETAS parameters on magnitude, rupture length, rupture width, and rupture area, we employ the p_{lm} value from a linear regression of the ETAS parameters with these mainshock characteristics. When the p_{lm} value of the slope coefficient of the linear regression is lower than a significance level of 0.01, the ETAS parameter is considered to be dependent on the variable in this study. In addition, given multiple tests of each ETAS parameter are carried out, the p_{lm} value is adjusted by the Bonferroni correction. The sign of the significance level of p_{lm} values is also included to show the correlation between the ETAS parameters and these mainshock characteristics. The result of the p_{lm} values from 18 robust ETAS estimates is shown in **Table 3**. Considering that the scaling law of rupture dimensions (e.g., Thingbaijam *et al.*, 2017) is a log-linear relationship between the logarithm of rupture dimensions and magnitude, we assess the p_{lm} values of α and γ with the logarithm of rupture dimensions, as shown in **Table 3**.

In **Table 3**, K_0 shows dependence on magnitude, rupture length, and rupture area of the largest earthquake in the sub-catalogs. K_0 grows with the magnitude, rupture length, and rupture area of the largest earthquake. The dependence of K_0 on magnitude and rupture dimensions might reflect the known bias from the isotropic spatial distribution, because the two largest K_0 are from two **M**9-class events with large rupture lengths and areas (Events 10 and 25 in Western Indonesia and Japan).

Overall, ETAS parameter results grouped by regions and magnitudes suggest: (1) the estimated values of K_0 and α are biased due to the anti-correlation of the productivity parameters and the isotropic spatial distribution in the ETAS parameter estimation; (2) sample size fluctuations due to varying target windows and high M_{cut} impact the c-value; (3) the median ETAS parameters of Papua New Guinea and South America are similar, which seems robust given the larger sample sizes and wider magnitude bins here than in other regions; (4) temporal parameters from Case 1 are consistent with observations from other studies. Although spatial parameters from Case 1 exhibit less variability, we believe *γ*- and *d*- values from Case 1 are biased as suggested by other researchers.

Case 2 - Long Time Period Catalogs with Fixed α

To reduce the bias of the productivity parameters due to the isotropic spatial distribution, a viable solution is to re-estimate ETAS parameters with fixed $\alpha = 2.3$ (Helmstetter *et al.*, 2006; Hainzl *et al.*, 2013). The fixed α corresponds to b-value = 1 assuming the magnitude frequency distribution is independent of the mainshock magnitude (Felzer *et al.*, 2004). Recent studies have investigated ETAS parameters after α is fixed at 2.3. K_0 and d-values decrease, whereas the other parameters increase (Seif *et al.*, 2017; Zhang *et al.*, 2018).

This subsection investigates (1) the difference of the ETAS parameters between Case 1 with free α and Case 2 with fixed α, and (2) the variation of the ETAS parameters with regions and the largest magnitudes in Case 2. Since Case 2 uses the same sub-catalogs as Case 1, to evaluate the goodness-of-fit of the ETAS model to the catalogs and to interpret the changes of estimates after the α-value is fixed, we first present the residual analysis and Akaike Information Criterion (AIC) of Cases 1 and 2. Next, we discuss the results of the ETAS parameters of Case 2, in comparison with those for Case 1.

Residual Analysis of Cases 1 and 2

To assess the goodness-of-fit of the calibrated models to the catalogs, we conduct a residual analysis for the ETAS model fitting. Detailed results of Cases 1 and 2 are provided in the electronic supplement (see **Figures S1-S18** available in the electronic supplements to this article). The 99% error bound of Kolmogorov-Smirnov statistics is also included as suggested by Ogata (1988). There are four main observations. First, 8 out of 18 fitted sub-catalogs are within the 99% confidence bounds in Cases 1 and 2. The residual analysis of the other 10 sub-catalogs shows potentially significant discrepancies between the calibrated ETAS model and seismicity data, which can be related to the large mainshock-aftershock sequences and temporal fluctuations of the background seismicity in the observed catalogs (Harte, 2012; Bansal and Ogata, 2013; Hainzl *et al.*, 2013). These should be investigated further to understand how the ETAS model (or its parameter estimation) can be improved. However, statistical forecasting after a megathrust earthquake involves much greater fluctuations than in retrospective fitting, i.e. the model can still be useful for the purpose of aftershock hazard and risk analysis with appropriate consideration of the anisotropy of the aftershocks and parameter selection (e.g., Zhang *et al.* 2018).

Second, all **M**9-class sub-catalog analyses are outside the 99% confidence bounds during the mainshock-aftershock sequences for both Cases 1 and 2 and thus fail the formal residual analysis test. This might show the spatial and temporal characteristics of the **M**9-class event sub-catalogs are different from the ETAS model with an isotropic spatial distribution. The model tends to underpredict the aftershock productivity of large earthquakes, as expected in Case 1 when the α-value is biased towards small values because of anisotropic aftershock distributions. Similar observations were reported by Harte (2012) and Kumazawa *et al.* (2014).

Third, by fixing α in Case 2 improvements in fitting mainshock-aftershock sequences can only be observed for some sub-catalogs (Events 5, 16, and 34), while no significant changes are seen for other sub-catalogs. Events with better fitting are all **M**8-class events from South America and Eastern Indonesia. This suggests that effects other than the isotropic assumption might affect the residual fitting, e.g., the stochastic declustering.

Fourth, the number of background events of Case 1 is systematically smaller than in Case 2 with fixed α. In other words, a smaller number of events are defined as triggered events by the stochastic declustering in Case 2 than in Case 1. This might result from a combined effect of the isotropic spatial aftershock distribution and the stochastic declustering.

We also compare the log-likelihood values and AIC of Case 1 with Case 2 (see **Table S2** available in the electronic supplements to this article). Case 1 with an additional free parameter α has a better performance than Case 2 in terms of AIC, which is consistent with the observation from Hainzl *et al.* (2013). We emphasize that fixing α improves the aftershock productivity forecast, which is important for hazard, at the cost of a lower likelihood of retrospective data.

ETAS Parameter Results of Case 2

Because of the known bias of α, the ETAS parameters are re-estimated with α = 2.3, as recommended by Seif *et al.* (2017) and others. Similarly to Case 1, we do not observe systematic ETAS parameter variations with region, and therefore provide parameter results classified by region and the boxplots of the ETAS parameters in **Appendix B**. **Figure 4** shows the parameter estimates of Case 2 with fixed α classified by the largest magnitudes in sub-catalogs. To have a clear comparison between Cases 1 and 2, the former results are plotted in grey without numbering.

In **Figure 4**(a), the K_0 values associated with **M**7.5-class sub-catalogs (Events 20 and 31 in New Zealand and Papua New Guinea) and **M**9-class sub-catalogs (Events 10 and 25 in Indonesia and Japan) are larger than 0.14 and 0.1, respectively, leading to supercritical processes for these sub-catalogs. The supercritical process means the average number of aftershocks per earthquake is larger than 1 (Seif *et al.*, 2017). Supercritical ETAS simulations can lead to aftershock number singularities in finite time (Helmstetter and Sornette, 2002). These K_0 estimates might be overestimated, because the cumulative number of observed events in the transformed time domain from Events 10, 20, 25, and 31 that is calculated based on the estimated ETAS parameters is larger than the theoretical number of events in the residual analysis. The rest of K_0 values are more robust than Case 1 with α free.

All *c*-values and 14 out of 18 *p*-values increase from Case 1 to Case 2, similar to results by Seif *et al.* (2017) and Zhang *et al.* (2018). This might be related to the increased background rates in Case 2. As indicated in the **Residual Analysis of Cases 1 and 2 section**, the total number of background events of Case 1 is systematically smaller than Case 2. Therefore, a smaller number of events are used to fit the temporal parameters in Case 2, which might lead to a quicker decay (large *p*-value) in time than Case 1. In addition, as concluded in the **Regional Dependence of ETAS Parameters in Case 1 section**, the *c* estimates may be biased by the sample size, therefore all *c*-values are increased in Case 2.

γ-values systematically increase in Case 2 leading to smaller *d*-values. The γ- and *d*-values from Case 2 are within the range of expected parameters from the literature (Seif *et al.*, 2017; Zhang *et al.*, 2018), reflecting a better fit with the conventional isotropic spatial distribution. An unusual $\gamma = 3.7$ of Event 10 is observed; this is larger than the maximum theoretical value $\gamma = 2.3$ discussed in the **Regional Dependence of ETAS Parameters in Case 1 section**. 14 out of 18 *q*-values are decreased, which is inconsistent with an increased *q*-value as reported in other studies (Seif *et al.*, 2017; Zhang *et al.*, 2018). This suggests other sources affect *q*, which could be the relatively large location errors of the global earthquake catalogs (Console *et al.*, 2003).

We evaluate the p_{lm}-value for the ETAS parameters of Case 2 from 18 estimates in **Table 4**. The previously observed co-dependencies on magnitude and rupture dimensions (**Table 3**) are not robust with respect to fixing *α*. The productivity and spatial parameters from Case 2 with fixed *α* are consistent with the observations from other studies and show more robust estimates than Case 1. The temporal parameters of Case 2 are also associated with relatively small variability; however, this might be due to biases by the sample size and stochastic declustering.

Case 3 - Individual Sequences

Case 3 only has 10 robust estimations in total from individual sequences. Since the number of sub-catalogs with sufficient quality in each region is small, it is difficult to infer systematic regional variations of the ETAS parameter in Case 3. In **Figure 5**, we show the ETAS parameter results of Case 3 grouped by mainshock magnitudes. We further calculate the p_{lm}-values of the regressions of ETAS parameters of Case 3 with the 10 robust estimates on rupture dimensions and magnitude and show full results in **Appendix B**. We see no evidence that the ETAS parameters from individual sequences depend on magnitude or rupture dimensions (p_{lm}-values > 0.01).

According to **Figure 5** (a) and (b), K_0- and α-values of **M**7.5-7.9 earthquake sequences vary significantly (K_0 from 0.2 to 0.7 and α from 1.0 to 2.0), whereas the productivity terms of **M**8.0-9.0 events are robust with smaller uncertainties. Because of the missing aftershocks immediately after large mainshocks (Seif *et al.*, 2017), *c*-values based on individual sequences from Case 3 are likely to be biased which leads to the overestimation in comparison with Case 1. Only Events 7, 11, 17, and 26 in Japan, Indonesia, and Philippines have *p*-values less than 1.25, the other aftershock sequences display faster temporal decay. A possible explanation is the high M_{cut} in comparison with other studies (e.g., M_{cut} = 2 from Seif *et al.* (2017)): The events below M_{cut} in the tail of the temporal distribution are excluded, leading to an apparently fast decay of some sequences.

In **Figure 5** (e) and (g), the *d* and *q* of Case 3 have larger standard errors for **M**7.5-8.5 events, suggesting that the far-field earthquakes are not within our space-magnitude target window given the proximity of the mainshock magnitudes to the completeness threshold. In comparison with γ from Case 1 with the longer catalogs (**Figure 2** (f)), the sequence-based γ from **Figure 5** (f) is larger and closer to expected values. For example, γ of Case 3 from the 2004 Aceh-Andaman earthquake increases from 1.09 to 1.53 in **Figure 5** (f). This might indicate that the ETAS model considers the 2004 Aceh-Andaman earthquake sequence as several individual sequences.

Comparing the ETAS parameter estimates from Cases 1 to 3, four main observations are: (1) the parameter estimates from the longer catalogs (Cases 1 and 2) with smaller errors and less variability are more robust than those from individual sequences (Case 3). (2) From Case 1, K_0 appears to depend on magnitude and rupture dimensions, but this can be explained in terms of the known parameter correlations due to mathematical model formulation and the biases due to the effects of isotropic spatial aftershock distribution. (3) Given the range of variability of the estimated parameters, there is only weak evidence that ETAS parameters vary with the largest magnitude and region in Cases 1 and 2. (4) Although some moderate variability is observed (e.g. the productivity parameters in Case 1 with free α), the temporal parameters from Case 1 and the productivity and spatial parameters from Case 2 with fixed α show robust estimates consistent with prior studies (Ogata and Zhuang, 2006; Seif *et al.*, 2017; Zhang *et al.*, 2018).

It appears that a consistent comparison of ETAS parameters requires not only a uniform completeness threshold but also a similar maximum (observed) magnitude. This ensures similar sample sizes. The sub-catalog range of this study in the maximum observed magnitude is from 7.5 to 9.0, while other studies that focus on regional or local seismicity often have wider ranges of magnitudes. For example, Seif *et al.* (2017) used Californian and Italian catalogs with maximum magnitudes near **M**7.0 and M_{cut}=2. This five-magnitude unit range resulted in robust ETAS parameters. On the other hand, this study focuses on global subduction events with mainshock magnitudes **M**7.5-9.0 and M_{cut}=4.5 due to the (relatively) sparse global monitoring system. Therefore, only regions with **M**8.0-9.0 events have a similar magnitude range and robust ETAS parameter estimates.

ETAS Parameter Estimation of Multiple Subduction Earthquakes

To investigate the change of the ETAS parameters due to multiple large earthquakes occurring in the same region, parameters are re-estimated in enlarged spatial regions of offshore Indonesia, Japan, and Chile that included more than one large earthquake and their sequences. Estimates are summarized in **Table 5**.

Figure 6 shows nearly no changes in the ETAS parameters of **M**9-class events when additional large subduction earthquake sequences in broadly the same region are included. This indicates that the estimated ETAS parameters are not fluctuating abruptly over time within the same region. But the finding could also be a (less intriguing) result of the aftershock numbers being dominated by the largest **M**9.0 sequences. Subsequent, less productive sequences of smaller mainshocks might have different ETAS parameters but do not influence the overall estimates. Again, similar sample sizes and magnitude ranges are important for making such comparisons.

Global ETAS Parameters for M9-class Events and its Simulation

In this section, representative ETAS parameters are proposed for future **M**9-class events, and their performances are checked by comparing forward simulations with observed sequences of **M**9-class earthquakes. As pointed out in the Introduction, the ETAS simulation framework includes an anisotropic distribution for the first generation of aftershocks of **M**9-class earthquakes to match observed aftershock patterns better (Zhang *et al.*, 2018).

Global ETAS Parameters for M9-class Events

To find a representative set of ETAS parameters for future generic **M**9.0 sequences, we use the robust estimates of temporal parameters from Case 1 and productivity and spatial parameters from Case 2 based on the findings from the **Comparison of ETAS Parameters by Region and Magnitude section**. Due to the known parameter biases from the model formulation, the isotropic spatial distribution, and the sample size, the criteria to find an acceptable set of ETAS parameters for generic future **M**9.0 sequences are:

- Productivity terms should not be supercritical to avoid explosive ETAS simulations.
- To ensure the total seismicity rate is in the range of the observed sequence, only parameter estimates that result in acceptable residual analysis results (within 99% error bounds) are included for K_0 selection.
- Unusual and suspicious parameter estimates are excluded. For example, parameter sets with $q > 3$, $d > 50$, and $\gamma > 2.3$ or $\gamma < 1$ are not considered, which is consistent with the observations from other studies (Ogata and Zhuang, 2006; Chu *et al.*, 2011; Seif *et al.*, 2017).

Different parameter sets are selected based on the criteria above. The final set of the parameters is calculated from the median value of the selected sub-catalogs and the standard error is calculated following the same procedure as for boxplots in **Appendix B**. The final set of parameters with median values and stand errors is summarized in **Table 6**.

ETAS Simulations of M9-class Events

To show that the proposed global **M**9.0 ETAS parameters from the **Global ETAS Parameters for M9-class Events section** are consistent with previously observed sequences, we simulate the 2004 Aceh-Andaman, the 2010 Maule, and the 2011 Tohoku earthquake sequences using the framework developed by Zhang *et al.* (2018). The synthetic catalogs of **M**9-class earthquake sequences are generated based on the ETAS parameters (K_0 = 0.04±0.02, α = 2.3, c = 0.03±0.01, p = 1.21±0.08, γ =1.61±0.29, d = 23.48±18.17, and q = 1.68±0.55). The ETAS parameters are randomly sampled from a normal distribution (Schoenberg *et al.*, 2010). Other simulation input information is summarized in **Table 7**. Rupture dimensions are sampled from the scaling law by Thingbaijam *et al.* (2017) and the uncertainty of the mainshock source parameters is also considered by assuming a bounded uniform distribution for strike and dip angles. 10,000 simulations are performed for each sequence.

From **Figure 7**, **Figure 8**, and **Figure 9**, the observations of the 2004 Aceh-Andaman, 2010 Maule, and 2011 Tohoku earthquakes, especially within the first week of the mainshock, are in the ranges of the ETAS simulations. The spike on day 13 in **Figure 8** is the **M**6.9 Pichilemu earthquake followed by a **M**6.7 aftershock. The mean of the simulated daily numbers exceeds the aftershock numbers observed on day 1 after both the Aceh-Andaman and Maule mainshocks (**Figure 7** and **Figure 8**). The aftershocks on day 1 after Tohoku, on the other hand, are more numerous than the mean forecast (**Figure 9**(b)). This is related to the K_0-value. The numbers of **M**≥5.5 aftershocks of the 2004 Aceh-Andaman earthquake and the 2010 Maule earthquake on day 1 are approximately 40 for both sequences, while for the Tohoku sequence, the number of **M**≥5.5 aftershocks on day 1 is more than 100, noting that Zhang *et al.* (2018) reported K_0 = 0.064 for the Tohoku sequence. The K_0 estimated in this study thus represents the averaged case across different subduction regions. Importantly, the range of the forecasts captures the observed values.

Conclusions

This study investigated the global variability of the ETAS parameters in subduction regions that experienced **M**7.5+ megathrust earthquakes. Longer regional as well as shorter sequence-specific selections of the global NEIC earthquake catalog were prepared to calibrate the ETAS model. The results suggest that:

- The ETAS parameters from the longer catalogs (Cases 1 and 2) have smaller standard errors and are less variable than those of sequence-specific catalogs (Case 3), because the number of events in sequence-specific sub-catalogs of **M**7.5-8.5 earthquakes is relatively small given the high M_{cut} of the NEIC catalog.
- No obvious systematic regional dependency of parameters is observed in either Case 1 or 2. The median ETAS parameters of Papua New Guinea and South America are similar from Cases 1 and 2, which seems robust given the larger sample sizes and wider magnitude bins here than in other regions.
- A test of correlation between ETAS parameters and mainshock parameters revealed no statistically significant results, except for K_0 in Case 1, but we interpret the dependency as a result of known biases due to the ETAS model formulation, namely the assumed isotropic aftershock distribution.
- The variability of parameters estimated from multiple sequences (**M**9.0 and **M**8.0 events) in the same subduction zones (Indonesia, Chile, and Japan) is small, because the **M**9.0 sequences dominate the input catalogs and **M**8.0 sequences have a smaller impact on the parameter estimation.

On the basis of the estimated parameters with known biases due to the isotropic spatial distribution and an evaluation of their quality, ETAS parameters for future **M**9-class events are suggested: K_0 = 0.04±0.02, α = 2.3, c = 0.03±0.01, p = 1.21±0.08, γ =1.61±0.29, d = 23.48±18.17, and q = 1.68±0.55. Synthetic catalogs we generated using the suggested ETAS parameters are consistent with those observed during the 2004 Aceh-Andaman, the 2010 Maule, and the 2011 Tohoku earthquake sequences.

The limitations of this parameter estimation are noteworthy. (1) Aftershocks are modelled isotropically in space around mainshock epicenters, while observed aftershock patterns align with anisotropic mainshock rupture planes. ETAS models with an anisotropic spatial distribution (e.g., Ogata and Zhuang, 2006) should lead to less biased parameter estimates. (2) The standard error of each parameter in this study is estimated assuming other parameters are fixed. The covariance of the parameters is not explicitly included in this study. Therefore, the parameter uncertainty could be larger than the standard errors reported here, further supporting the inference that observed parameter variations are insignificant. (3) In this study we combined a quantitative statistical analysis with qualitative judgements to investigate the variability of ETAS parameters across different subduction-zone regions. However, developing a new model to find a remedy for the biases of ETAS parameters is beyond the scope of this paper. (4) The proposed standard errors of ETAS parameters for future **M**9.0 sequences are large, because the standard errors include the uncertainty of ETAS parameters from different regions.

Data and Resources

The JMA catalog is from http://www.data.jma.go.jp/svd/eqev/data/bulletin/hypo_e.html. (last accessed on January 20, 2017). The NEIC catalog is from https://earthquake.usgs.gov/data/pde.php (last accessed on November 18, 2018). The mainshock rupture models are from http://equake-rc.info/SRCMOD/ and https://earthquake.usgs.gov/earthquakes/browse/ (last accessed on September 7, 2018).

Acknowledgments

This project (M.J.W.) has received funding from the European Union's Horizon 2020 research and innovation program under grant agreement No 821115, Real-Time Earthquake Risk Reduction for a Resilient Europe (RISE). L.Z. and M.J.W. appreciate support from the London Mathematical Laboratory (http://lml.org.uk/). This research was also supported by the Southern California Earthquake Center (Contribution No. 9081). SCEC is funded by NSF Cooperative Agreement EAR-1600087 & USGS Cooperative Agreement G17AC00047. This work was supported by the Canada Research Chair in Multi-Hazard Risk Assessment program (950-232015) for K.G.

References

Bansal, A.R. and Y. Ogata (2013) A non-stationary epidemic type aftershock sequence model for seismicity prior to the December 26, 2004 M 9.1 Sumatra-Andaman Islands mega-earthquake, *J. Geophys. Res. Solid Earth* **118**, 616–629.

Béjar-Pizarro, M., D. Carrizo, A. Socquet, R. Armijo, S. Barrientos, F. Bondoux, S. Bonvalot, J. Campos, D. Comte, J.B. De Chabalier, and others (2010) Asperities and barriers on the seismogenic zone in North Chile: state-of-the-art after the 2007 M w 7.7 Tocopilla earthquake inferred by GPS and InSAR data, *Geophys. J. Int.* **183**, 390–406.

Bird, A.L. and M. Lamontagne (2015) Impacts of the October 2012 magnitude 7.8 earthquake near Haida Gwaii, Canada, *Bull. Seismol. Soc. Am.* **105**, 1178–1192.

Chu, A., F.P. Schoenberg, P. Bird, D.D. Jackson, and Y.Y. Kagan (2011) Comparison of ETAS parameter estimates across different global tectonic zones, *Bull. Seismol. Soc. Am.* **101**, 2323–2339.

Console, R., M. Murru, and A.M. Lombardi (2003) Refining earthquake clustering models, *J. Geophys. Res. Solid Earth* **108**, doi: 10.1029/2002JB002130.

Ebrahimian, H., F. Jalayer, D. Asprone, A.M. Lombardi, W. Marzocchi, A. Prota, and G. Manfredi (2014) A performance-based framework for adaptive seismic aftershock risk assessment, *Earthq. Eng. Struct. Dyn.* **43**, 2179–2197.

Farías, M., D. Comte, S. Roecker, D. Carrizo, and M. Pardo (2011) Crustal extensional faulting triggered by the 2010 Chilean earthquake: The Pichilemu Seismic Sequence, *Tectonics* **30**, doi: 10.1029/2011TC002888.

Felzer, K.R., R.E. Abercrombie, and G. Ekström (2004) A common origin for aftershocks, foreshocks, and multiplets, *Bull. Seismol. Soc. Am.* **94**, 88–98.

Field, E., K. Porter, and K. Milner (2017) A prototype operational earthquake loss model for California based on UCERF3-ETAS--a first look at valuation, *Earthq. Spectra* **33**, 1279–1299.

Fukushima, Y., Y. Takada, and M. Hashimoto (2013) Complex ruptures of the 11 April 2011 Mw 6.6 Iwaki earthquake triggered by the 11 March 2011 Mw 9.0 Tohoku earthquake, Japan, *Bull. Seismol. Soc. Am.* **103**, 1572–1583.

Hainzl, S. (2016) Apparent triggering function of aftershocks resulting from rate-dependent incompleteness of earthquake catalogs, *J. Geophys. Res. Solid Earth* **121**, 6499–6509.

Hainzl, S., A. Christophersen, and B. Enescu (2008) Impact of earthquake rupture extensions on parameter estimations of point-process models, *Bull. Seismol. Soc. Am.* **98**, 2066–2072.

Hainzl, S., O. Zakharova, and D. Marsan (2013) Impact of aseismic transients on the estimation of aftershock productivity parameters, *Bull. Seismol. Soc. Am.* **103**, 1723–1732.

Harte, D.S. (2012) Bias in fitting the ETAS model: A case study based on New Zealand seismicity, *Geophys. J. Int.* **192**, 390–412.

Hayes, G.P., E.K. Meyers, J.W. Dewey, R.W. Briggs, P.S. Earle, H.M. Benz, G.M. Smoczyk, H.E. Flamme, W.D. Barnhart, R.D. Gold, and others (2017) *Tectonic summaries of magnitude 7 and greater earthquakes from 2000 to 2015*,.

Helmstetter, A., Y.Y. Kagan, and D.D. Jackson (2006) Comparison of short-term and time-independent earthquake forecast models for southern California, *Bull. Seismol. Soc. Am.* **96**, 90–106.

Helmstetter, A., Y.Y. Kagan, and D.D. Jackson (2005) Importance of small earthquakes for stress transfers and earthquake triggering, *J. Geophys. Res. Solid Earth* **110**, doi: 10.1029/2004JB003286.

Helmstetter, A. and D. Sornette (2002) Subcritical and supercritical regimes in epidemic models of earthquake aftershocks, *J. Geophys. Res. Solid Earth* **107**, doi: 10.1029/2001JB001580.

Iervolino, I., E. Chioccarelli, M. Giorgio, W. Marzocchi, G. Zuccaro, M. Dolce, and G. Manfredi (2015) Operational (short-term) earthquake loss forecasting in Italy, *Bull. Seismol. Soc. Am.* **105**, 2286–2298.

Kagan, Y.Y. (2002) Aftershock zone scaling, *Bull. Seismol. Soc. Am.* **92**, 641–655.

Kagan, Y.Y. (2004) Short-term properties of earthquake catalogs and models of earthquake source, *Bull. Seismol. Soc. Am.* **94**, 1207–1228.

Kao, H., S.-J. Shan, and A.M. Farahbod (2015) Source characteristics of the 2012 Haida Gwaii earthquake sequence, *Bull. Seismol. Soc. Am.* **105**, 1206–1218.

Koketsu, K., K. Hikima, S. Miyazaki, and S. Ide (2004) Joint inversion of strong motion and geodetic data for the source process of the 2003 Tokachi-oki, Hokkaido, earthquake, *Earth, planets Sp.* **56**, 329–334.

Kumazawa, T., Y. Ogata, and others (2014) Nonstationary ETAS models for nonstandard earthquakes, *Ann. Appl. Stat.* **8**, 1825–1852.

Lay, T., H. Kanamori, C.J. Ammon, A.R. Hutko, K. Furlong, and L. Rivera (2009) The 2006-

-2007 Kuril Islands great earthquake sequence, *J. Geophys. Res. Solid Earth* **114**, doi: 10.1029/2008JB006280.

Lay, T., L. Ye, H. Kanamori, Y. Yamazaki, K.F. Cheung, K. Kwong, and K.D. Koper (2013) The October 28, 2012 Mw 7.8 Haida Gwaii underthrusting earthquake and tsunami: Slip partitioning along the Queen Charlotte fault transpressional plate boundary, *Earth Planet. Sci. Lett.* **375**, 57–70.

Lombardi, A.M. (2017a) SEDA: A software package for the Statistical Earthquake Data Analysis, *Sci. Rep.* **7**, 44171, doi: 10.1038/srep44171.

Lombardi, A.M. (2017b) The epistemic and aleatory uncertainties of the ETAS-type models: an application to the Central Italy seismicity, *Sci. Rep.* **7**, 11812, doi: 10.1038/s41598-017-11925-3.

Luco, N. (2002) Probabilistic seismic demand analysis, SMRF connection fractures, and near-source effects, *Ph.D. thesis*, Stanford University, Standford, California.

Luttrell, K.M., X. Tong, D.T. Sandwell, B.A. Brooks, and M.G. Bevis (2011) Estimates of stress drop and crustal tectonic stress from the 27 February 2010 Maule, Chile, earthquake: Implications for fault strength, *J. Geophys. Res. Solid Earth* **116**, doi: 10.1029/2011JB008509.

Mai, P.M. and K.K.S. Thingbaijam (2014) SRCMOD: An online database of finite-fault rupture models, *Seismol. Res. Lett.* **85**, 1348–1357.

Marzocchi, W. and L. Sandri (2003) A review and new insights on the estimation of the b-valueand its uncertainty, *Ann. Geophys.* doi: 10.4401/ag-3472.

Nanjo, K.Z., B. Enescu, R. Shcherbakov, D.L. Turcotte, T. Iwata, and Y. Ogata (2007) Decay of aftershock activity for Japanese earthquakes, *J. Geophys. Res. Solid Earth* **112**, doi: 10.1029/2006JB004754.

Narteau, C., S. Byrdina, P. Shebalin, and D. Schorlemmer (2009) Common dependence on stress for the two fundamental laws of statistical seismology, *Nature* **462**, 642–645.

Natawidjaja, D.H., K. Sieh, M. Chlieh, J. Galetzka, B.W. Suwargadi, H. Cheng, R.L. Edwards, J.-P. Avouac, and S.N. Ward (2006) Source parameters of the great Sumatran megathrust earthquakes of 1797 and 1833 inferred from coral microatolls, *J. Geophys. Res. Solid Earth* **111**, doi: 10.1029/2005JB004025.

Nicolis, O., M. Chiodi, and G. Adelfio (2015) Windowed ETAS models with application to the Chilean seismic catalogs, *Spat. Stat.* **14**, 151–165.

Ogata, Y. (1988) Statistical models for earthquake occurrences and residual analysis for point processes, *J. Am. Stat. Assoc.* **83**, 9–27.

Ogata, Y. and J. Zhuang (2006) Space-time ETAS models and an improved extension, *Tectonophysics* **413**, 13–23.

Page, M.T., N. Van Der Elst, J. Hardebeck, K. Felzer, and A.J. Michael (2016) Three ingredients for improved global aftershock forecasts: Tectonic region, time-dependent catalog incompleteness, and intersequence variability, *Bull. Seismol. Soc. Am.* **106**, 2290–2301.

Rhie, J., D. Dreger, R. Bürgmann, and B. Romanowicz (2007) Slip of the 2004 Sumatra--Andaman earthquake from joint inversion of long-period global seismic waveforms and GPS static offsets, *Bull. Seismol. Soc. Am.* **97**, S115--S127.

Ryder, I., A. Rietbrock, K. Kelson, R. Bürgmann, M. Floyd, A. Socquet, C. Vigny, and D. Carrizo (2012) Large extensional aftershocks in the continental forearc triggered by the 2010 Maule earthquake, Chile, *Geophys. J. Int.* **188**, 879–890.

Schoenberg, F.P., A. Chu, and A. Veen (2010) On the relationship between lower magnitude thresholds and bias in epidemic-type aftershock sequence parameter estimates, *J. Geophys. Res. Solid Earth* **115**, doi: 10.1029/2009JB006387.

Seif, S., A. Mignan, J.D. Zechar, M.J. Werner, and S. Wiemer (2017) Estimating ETAS: the effects of truncation, missing data, and model assumptions, *J. Geophys. Res. Solid Earth* **122**, 449–469.

Shcherbakov, R., K. Goda, A. Ivanian, and G.M. Atkinson (2013) Aftershock statistics of major subduction earthquakes, *Bull. Seismol. Soc. Am.* **103**, 3222–3234.

Shcherbakov, R., D.L. Turcotte, and J.B. Rundle (2004) A generalized Omori's law for earthquake aftershock decay, *Geophys. Res. Lett.* **31**, doi: 10.1029/2004GL019808.

Shi, Y. and B.A. Bolt (1982) The standard error of the magnitude-frequency b value, *Bull. Seismol. Soc. Am.* **72**, 1677–1687.

Sornette, D. and M.J. Werner (2005a) Apparent clustering and apparent background earthquakes biased by undetected seismicity, *J. Geophys. Res. Solid Earth* **110**, doi: 10.1029/2005JB003621.

Sornette, D. and M.J. Werner (2005b) Constraints on the size of the smallest triggering earthquake from the epidemic-type aftershock sequence model, Båth's law, and observed aftershock sequences, *J. Geophys. Res. Solid Earth* **110**, doi: 10.1029/2004JB003535.

Storchak, D.A., J. Schweitzer, and P. Bormann (2003) The IASPEI standard seismic phase list, *Seismol. Res. Lett.* **74**, 761–772.

Thingbaijam, K.K.S. and P. Martin Mai (2016) Evidence for truncated exponential probability distribution of earthquake slip, *Bull. Seismol. Soc. Am.* **106**, 1802–1816.

Thingbaijam, K.K.S., P. Martin Mai, and K. Goda (2017) New empirical earthquake source-scaling laws, *Bull. Seismol. Soc. Am.* **107**, 2225–2246.

Toda, S., R.S. Stein, and J. Lin (2011) Widespread seismicity excitation throughout central Japan following the 2011 M=9.0 Tohoku earthquake and its interpretation by coulomb stress transfer, *Geophys. Res. Lett.* **38**, doi: 10.1029/2011GL047834.

Toda, S. and H. Tsutsumi (2013) Simultaneous reactivation of two, subparallel, inland normal faults during the Mw 6.6 11 April 2011 Iwaki earthquake triggered by the Mw 9.0 Tohoku-oki, Japan, earthquake, *Bull. Seismol. Soc. Am.* **103**, 1584–1602.

Utsu, T., Y. Ogata, and S.R. Matsu'ura (1995) The centenary of the Omori formula for a decay law of aftershock activity., *J. Phys. Earth* **43**, 1–33.

Wang, K. and A.M. Tréhu (2016) Invited review paper: Some outstanding issues in the study of great megathrust earthquakes—The Cascadia example, *J. Geodyn.* **98**, 1–18.

Wang, Q., D.D. Jackson, and J. Zhuang (2010) Missing links in earthquake clustering models, *Geophys. Res. Lett.* **37**, doi: 10.1029/2010GL044858.

Wei, S., R. Graves, D. Helmberger, J.-P. Avouac, and J. Jiang (2012) Sources of shaking and flooding during the Tohoku-Oki earthquake: A mixture of rupture styles, *Earth Planet. Sci. Lett.* **333**, 91–100.

Werner, M.J. (2007) On the fluctuations of seismicity and uncertainties in earthquake catalogs: Implications and methods for hypothesis testing, *Ph.D. thesis*, University of California, Los Angeles, California.

Wetzler, N., E.E. Brodsky, and T. Lay (2016) Regional and stress drop effects on aftershock productivity of large megathrust earthquakes, *Geophys. Res. Lett.* **43**, doi: https://doi.org/10.1002/2016GL071104.

Woessner, J. and S. Wiemer (2005) Assessing the quality of earthquake catalogues: Estimating the magnitude of completeness and its uncertainty, *Bull. Seismol. Soc. Am.* **95**, 684–698.

Yagi, Y. and Y. Fukahata (2011) Introduction of uncertainty of Green's function into waveform inversion for seismic source processes, *Geophys. J. Int.* **186**, 711–720.

Yagi, Y., T. Mikumo, J. Pacheco, and G. Reyes (2004) Source rupture process of the Tecom{á}n, Colima, Mexico earthquake of 22 January 2003, determined by joint inversion of teleseismic body-wave and near-source data, *Bull. Seismol. Soc. Am.* **94**,

1795–1807.
Ye, L., T. Lay, and H. Kanamori (2012) Intraplate and interplate faulting interactions during the August 31, 2012, Philippine Trench earthquake (Mw 7.6) sequence, *Geophys. Res. Lett.* **39**, doi: 10.1029/2012GL054164.
Zakharova, O., S. Hainzl, D. Lange, and B. Enescu (2017) Spatial variations of aftershock parameters and their relation to geodetic slip models for the 2010 Mw8. 8 Maule and the 2011 Mw9. 0 Tohoku-oki earthquakes, *Pure Appl. Geophys.* **174**, 77–102.
Zaliapin, I. and Y. Ben-Zion (2016) A global classification and characterization of earthquake clusters, *Geophys. J. Int.* **207**, 608–634.
Zhang, L., M.J. Werner, and K. Goda (2018) Spatiotemporal seismic hazard and risk assessment of aftershocks of M 9 megathrust earthquakes, *Bull. Seismol. Soc. Am.* **108**, 3313–3335.
Zhuang, J., Y. Ogata, and D. Vere-Jones (2002) Stochastic declustering of space-time earthquake occurrences, *J. Am. Stat. Assoc.* **97**, 369–380.

Full mailing address for each author

Lizhong Zhang
Queens Building
Department of Civil Engineering
University of Bristol
University Walk, Bristol, BS8 1TR
United Kingdom

Maximilian J. Werner
Wills Memorial Building
School of Earth Sciences
University of Bristol
Queens Road, Bristol, BS8 1RJ
United Kingdom

Katsuichiro Goda
Biological & Geological Sciences Building, Room 1076
Department of Earth Sciences
The University of Western Ontario
1151 Richmond St. N. London, ON N6A 5B7
Canada

Tables

Table 1. Summary of three cases of temporal auxiliary and target windows.

Cases 1 and 2		Case 3 (individual sequences of triggered events are analysed)					
		$7.5 \le M < 8$		$8.1 \le M < 8.7$		$M \ge 8.7$	
Auxiliary window	Target window	Auxiliary window	Target window	Auxiliary window	Target window	Auxiliary window	Target window
5 years	31 years	0.5 year	1 year	1 year	2 years	2 years	4 years

Table 2. Summary of the selected large subduction earthquakes.

Earthquake catalog								Mainshock rupture model			Long time windows- Cases 1 and 2 from Table 1.			Subduction sequences - Case 3 from Table 1.		
Index	Date/Time (UTC)	**M**	Region	Faulting style	Latitude °	Longitude °	Depth (km)	Reference	Effective length (km)	Effective Width (km)	M_c	*b*-value	Number of events M≥ 4.5	M_c	*b*-value	Number of events **M**≥4.5
1	11/16/2000 07:42	7.8	Papua New Guinea	Reverse (thrust)	-5.23	153.1	30	USGS	108	100	4.5	0.95±0.016	3105	4.6	0.96±0.043	567
2	11/17/2000 21:01	7.8	Papua New Guinea	Reverse (thrust)	-5.5	151.78	33	USGS	132	87.6	4.5	0.95±0.015	3465	4.6	0.93±0.042	543
3	06/23/2001 20:33	8.4	Peru	Reverse (thrust)	-16.27	-73.64	33	USGS	252	208	4.9	1.10±0.050	1215	4.6	0.96±0.058	299
4	07/07/2001 09:38	7.6	Peru	Reverse (thrust)	-17.54	-72.08	33	USGS	140	91.8	4.9	1.21±0.083	479	4.7	1.15±0.101	182
5	03/05/2002 21:16	7.5	Philippines	Reverse (thrust)	6.03	124.25	31	USGS	105	98	4.4	0.99±0.047	322	4.3	1.04±0.121	58
6	01/22/2003 02:06	7.6	Mexico	Reverse (thrust)	18.77	–104.10	24	Yagi *et al.*, 2004	70	85	3.9	0.88±0.047	94	4	1.20±0.281	8
7	09/25/2003 19:50	8.3	Japan	Reverse (thrust)	41.82	143.91	27	Koketsu *et al.*, 2004	120	100	4.6	1.00±0.028	1391	4.4	0.80±0.043	269
8	11/17/2003 06:43	7.8	Alaska	Reverse (thrust)	51.15	178.65	33	USGS	132	140.4	4.5	0.90±0.025	1212	4.1	0.91±0.056	116
9	11/11/2004 21:26	7.5	Indonesia	Reverse (thrust)	–8.15	124.87	10	USGS	84	72.8	4.4	0.95±0.047	329	4.3	0.97±0.074	111
10	12/26/2004 0:58	9.0	Indonesia	Reverse (thrust)	3.3	95.98	30	Rhie *et al.*, 2007	970	200	4.5	1.11±0.015	5526	4.5	1.12±0.019	3298
11	03/28/2005 16:09	8.6	Indonesia	Reverse (thrust)	2.09	97.11	30	CALTECH*	380	192	4.5	1.11±0.017	4275	4.5	1.21±0.027	2077
12	7/17/2006 8:19	7.7	Indonesia	Reverse (thrust)	–9.28	107.42	20	Yagi and Fukahata, 2011	220	140	4.7	1.18±0.041	1089	4.8	1.38±0.103	348
13	11/15/2006 11:14	8.3	Kuril Islands	Reverse (thrust)	46.59	153.27	10	Lay *et al.*, 2009	240	100	4.6	1.14±0.021	3279	4.5	1.21±0.036	1077
14	1/21/2007 11:27	7.5	Indonesia	Reverse (thrust)	1.07	126.28	22	USGS	165	56.32	4.6	1.03±0.018	3119	4.6	1.08±0.061	345
15	04/01/2007 20:39	8.1	Solomon Islands	Reverse (thrust)	–8.47	157.04	24	CALTECH	285	80	4.5	0.92±0.015	3408	4.6	1.02±0.045	593
16	8/15/2007 23:40	8	Peru	Reverse (thrust)	–13.39	–76.60	39	CALTECH	168	160	4.4	0.89±0.034	509	4.2	0.75±0.051	112
17	09/12/2007 11:10	8.5	Indonesia	Reverse (thrust)	–4.44	101.37	34	CALTECH	342	208	4.7	1.05±0.022	3149	4.4	0.82±0.027	634
18	11/14/2007 15:40	7.7	Chile	Reverse (thrust)	–22.25	–69.89	40	Béjar-Pizarro *et al.*, 2010	210	98	4.2	0.76±0.016	1145	5.2	0.75±0.132	115

*California Institute of Technology

19	01/03/2009 19:43	7.7	Indonesia	Reverse (thrust)	–0.41	132.89	17	USGS	96	78	4.5	0.99±0.052	329	4.6	1.10±0.100	173
20	07/15/2009 9:22	7.8	New Zealand	Reverse (thrust)	–45.76	166.56	12	USGS	88	72	4.2	0.93±0.042	269	4.5	1.16±0.114	118
21	02/27/2010 6:34	8.8	Chile	Reverse (thrust)	–36.12	–72.90	23	Luttrell *et al.*, 2011	520	177.3	4.3	0.97±0.012	4285	4.6	1.10±0.029	1737
22	04/06/2010 22:15	7.8	Indonesia	Reverse (thrust)	2.38	97.05	31	USGS	144	156	5.3	0.88±0.069	2008	4.1	0.78±0.057	85
23	06/12/2010 19:26	7.5	Indonesia	Oblique Reverse	7.88	91.94	35	USGS	78	58	4.2	0.87±0.049	157	4.5	1.05±0.201	40
24	10/25/2010 14:42	7.8	Indonesia	Reverse (thrust)	–3.49	100.08	20	USGS	195	140	4.6	0.99±0.028	1579	4.5	1.12±0.088	175
25	03/11/2011 05:46	9	Japan	Reverse (thrust)	38.3	142.37	29	Wei *et al.*, 2012	450	200	4.5	1.08±0.010	10519	5	1.05±0.032	5022
26	8/31/2012 12:47	7.6	Philippines	Oblique Reverse	10.81	126.64	28	USGS	72	66	4.7	1.40±0.057	897	4.4	1.12±0.066	236
27	09/05/2012 14:42	7.6	Costa Rica	Reverse (thrust)	10.09	–85.32	35	USGS	110	88	4.8	0.80±0.060	379	4.3	1.17±0.220	32
28	10/28/2012 3:04	7.8	BC, Canada	Oblique Reverse	52.79	–132.10	14	Lay *et al.*, 2013	144	54	4	0.76±0.036	171	4	0.87±0.060	80
29	02/06/2013 01:12	8	Solomon Islands	Reverse (thrust)	–10.80	165.11	24	USGS	221	143	4.5	0.87±0.014	3155	4.6	1.02±0.039	723
30	04/01/2014 23:46	8.2	Chile	Reverse (thrust)	–19.61	–70.77	25	CALTECH	240	160	4.8	1.03±0.038	1313	4.4	0.95±0.043	409
31	4/19/2014 13:28	7.5	Papua New Guinea	Reverse (thrust)	–6.75	155.02	44	USGS	56	68	4.5	0.95±0.025	1267	4.4	1.06±0.050	356
32	3/29/2015 23:48	7.5	Papua New Guinea	Reverse (thrust)	–4.73	152.56	41	USGS	132	102	4.5	0.95±0.016	3441	4.3	0.98±0.041	343
33	05/05/2015 01:44	7.5	Papua New Guinea	Reverse (thrust)	–5.46	151.88	55	USGS	110	110	4.5	0.95±0.015	3375	4.6	1.07±0.070	316
34	9/16/2015 22:54	8.3	Chile	Reverse (thrust)	–31.57	–71.67	22	USGS	216	140.8	4.2	0.97±0.014	2421	4.2	1.00±0.029	623
35	04/16/2016 23:58	7.8	Ecuador	Reverse (thrust)	0.38	-79.92	20	USGS	154	140	5.4	0.81±0.113	262	4.1	0.70±0.055	79
36	12/25/2016 14:22	7.6	Chile	Reverse (thrust)	-43.41	-73.94	38	USGS	96	56	4	0.76±0.102	24	4.1	0.99±0.273	11

Table 3. Summary of the p_{lm} values of ETAS parameters for Case 1 (bold indicates statistically significant dependency and the "+" sign of the p_{lm} values indicates the correlation between the ETAS parameters and the earthquake characteristics).

	K_0	α	c	p	d	γ	q
Magnitude	**+0.0011**	0.1284	0.1127	0.0132	1.0000	1.0000	0.3666
Rupture length	**+0.0046**	0.0231	0.1380	0.1057	0.9865	0.8686	0.2500
Rupture width	0.1417	0.4251	0.6898	0.6041	0.8728	0.4162	0.9735
Rupture area	**+0.0035**	0.1761	0.2258	0.0936	0.7153	0.2788	0.2282

Table 4. Summary of the p_{lm} values of ETAS parameters for Case 2 (Boldface indicates significant co-dependence).

	K_0	α	c	p	d	γ	q
Magnitude	0.1724	0	0.3709	0.0429	1.0000	0.0833	1.0000
Rupture length	0.0424	0	0.2032	0.2327	0.9417	0.0124	1.0000
Rupture width	1.0000	0	1.0000	0.8790	1.0000	0.4805	1.0000
Rupture area	0.0288	0	0.2623	0.1835	1.0000	0.0414	1.0000

Table 5. Summary of the estimated ETAS parameters of multiple subduction earthquakes with time windows 1981-2017.

	Indonesia A	Indonesia B	Indonesia C	Chile A	Chile B	Japan A	Japan B
Event index	10	37 (Events 10, 11, and 22)	38 (Events 10, 11, 17, 22, and 24)	21	39 (Events 21 and 34)	25	40 (Events 7 and 25)

Table 6. Suggested ETAS parameters for future **M**9.0 events.

	K_0 (event/day)	α (magnitude^{-1})	c (day)	p	d (km^2)	γ (magnitude^{-1})	q
Median values	0.04	2.3	0.03	1.21	23.48	1.61	1.68
Standard errors	0.02	0	0.01	0.08	18.17	0.29	0.55

Table 7. Summary of the mainshock source parameters of the ETAS simulations

	Rupture length (km)	Rupture width (km)	Length-width ratio	Strike angle	Dip angle	Mainshock epicentre	Mainshock magnitude
2004 Ache-Andaman event	1100-1300	200-300	4.5-5	344°-346°	15°-16°	93.5°E, 8.2°N	9.1
2010 Maule event	550-580	140-200	3-4	16°-18°	17°-18°	-72.7°W, -35.7°S	8.8
2011 Tohoku event	450-550	200-240	2-3	202°-210°	10°-12°	142.2°E, 37.7°N	9.0

List of Figure Captions

Figure 1. Map of earthquake locations with $M \geq 7.5$. Earthquakes are grouped by regions, which are Japan (JPN), Eastern Indonesia (EI), Papua New Guinea (PNG), Western Indonesia (WI), North America (NA), Central America (CA), and South America (SA). The numbers in parentheses correspond to the indices in **Table 2**.

Figure 2. ETAS parameter estimates classified by region for Case 1 based on long-time catalogs with free α (SA: South America, NA: North America, JPN: Japan, PNG: Papua New Guinea, EI: Eastern Indonesia, WI: Western Indonesia, and NZ: New Zealand).

Figure 3. Anti-correlation between estimated K_0 and α parameters, color-coded by the ratios of rupture length to width of the largest earthquakes within the sub-catalogs.

Figure 4. ETAS parameter results of Case 2 with fixed α classified by the largest magnitudes in sub-catalogs (ETAS parameter results of Case 1 are plotted without numbering for comparison).

Figure 5. ETAS parameter results classified by mainshock magnitudes for Case 3 based on individual sequences.

Figure 6. Parameter results from the sub-catalogs with multiple subduction earthquakes in Indonesia, Chile, and Japan.

Figure 7. Comparison of observed and simulated M5.5+ aftershocks of the 2004 Aceh-Andaman earthquake: (a) magnitude frequency distribution in square root scale during the first three months, (b) daily number of events during the first 30 days, (c) observed 2D aftershock histograms during the first three months, (d) a simulated 2D aftershock histogram over the same period.

Figure 8. Comparison of observed and simulated M5.5+ aftershocks after the 2010 Maule earthquake: (a) magnitude frequency distribution during the first three months, (b) daily number of events during the first 30 days, (c) observed 2D aftershock histogram during the first three months, (d) a simulated 2D aftershock histogram over the same period.

Figure 9. Comparison of observed and simulated M5.5+ aftershocks after the 2011 Tohoku earthquake: (a) magnitude frequency distribution in square root scale during the first three months, (b) daily number of events during the first 30 days, (c) observed 2D aftershock histogram during the first three months, (d) a simulated 2D aftershock histogram during the first three months.

Figures

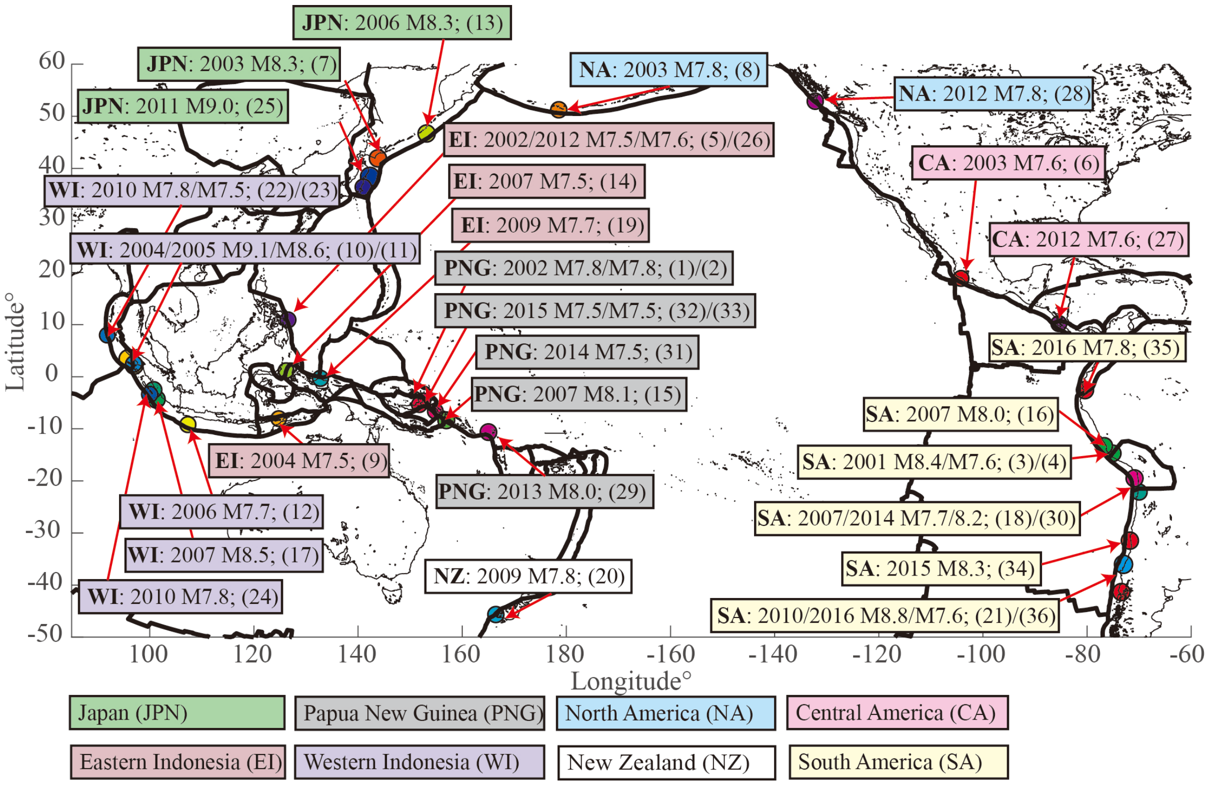

Figure 1. Map of earthquake locations with M≥7.5. Earthquakes are grouped by regions, which are Japan (JPN), Eastern Indonesia (EI), Papua New Guinea (PNG), Western Indonesia (WI), North America (NA), Central America (CA), and South America (SA). The numbers in parentheses correspond to the indices in **Table 2**.

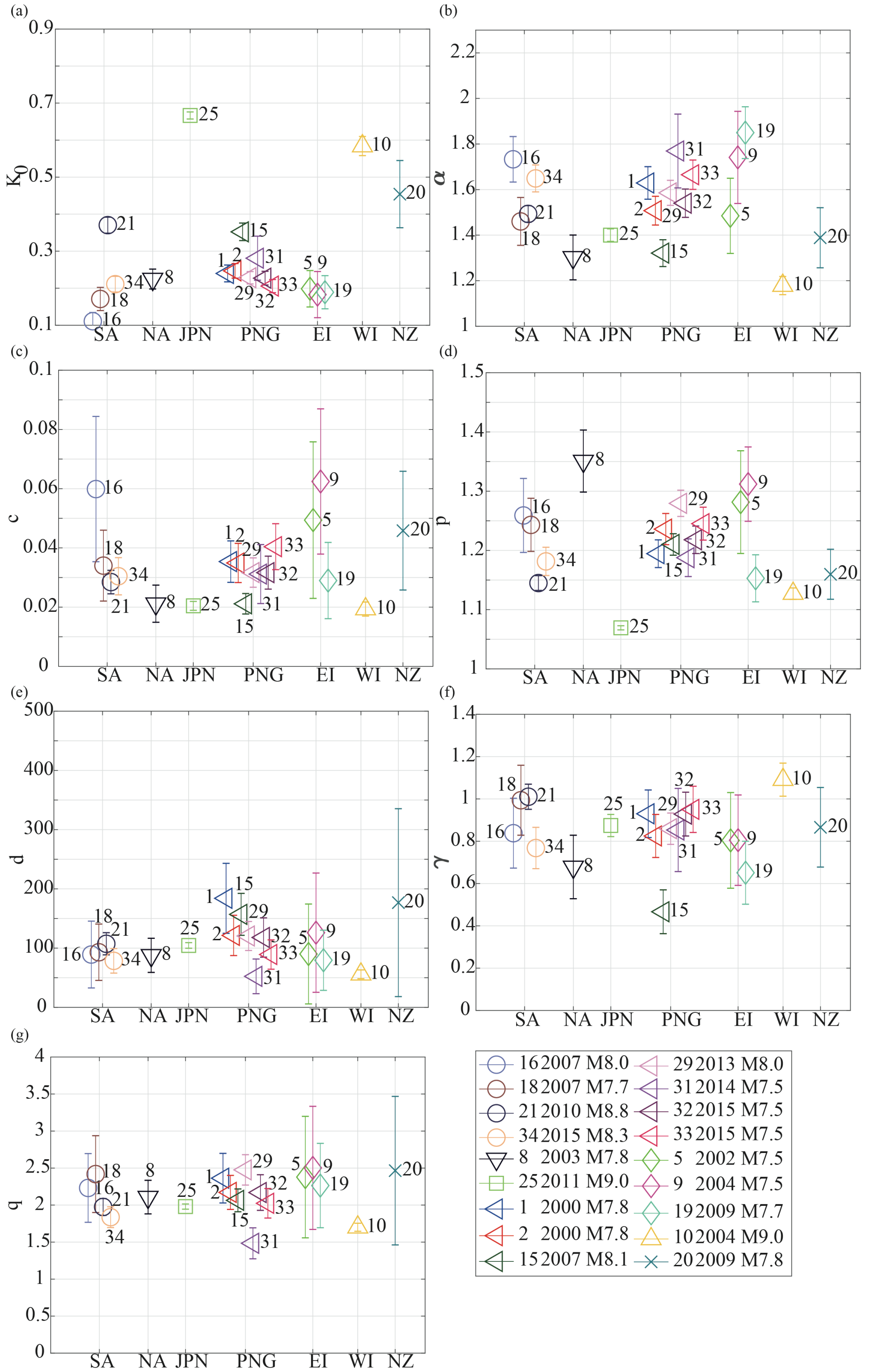

Figure 2. ETAS parameter estimates classified by region for Case 1 based on long-time catalogs with free α (SA: South America, NA: North America, JPN: Japan, PNG: Papua New Guinea, EI: Eastern Indonesia, WI: Western Indonesia, and NZ: New Zealand).

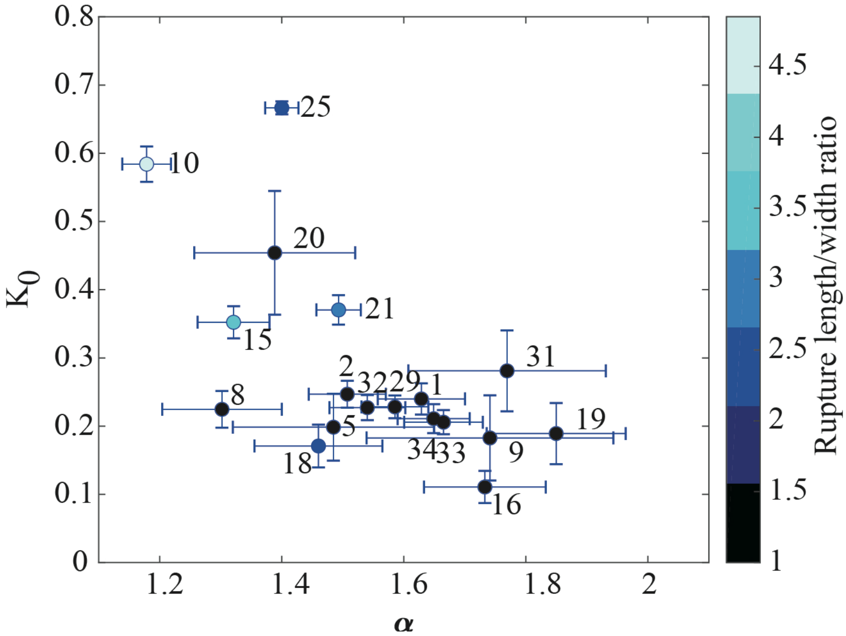

Figure 3. Anti-correlation between estimated K_0 and α parameters, color-coded by the ratios of rupture length to width of the largest earthquakes within the sub-catalogs.

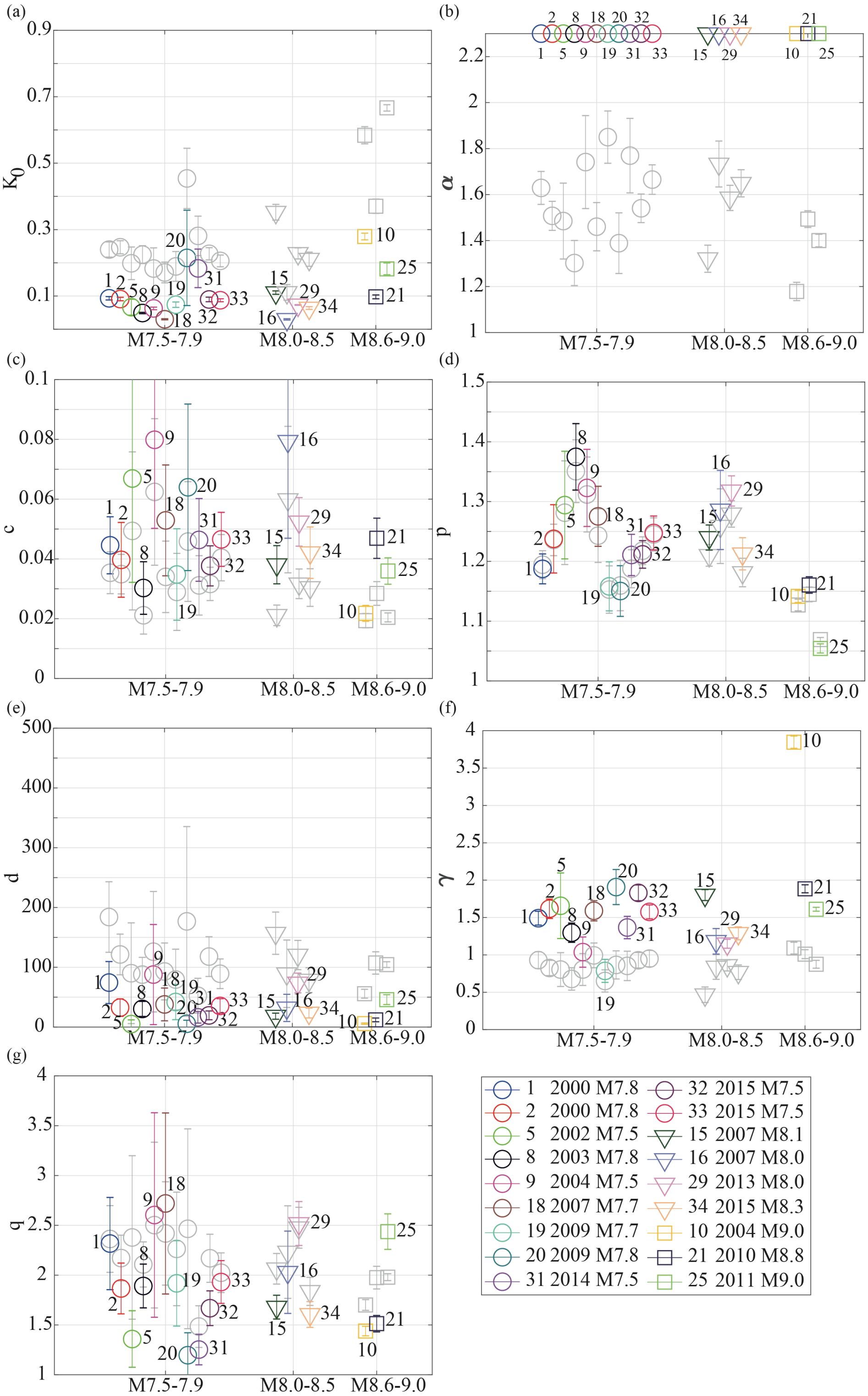

Figure 4. ETAS parameter results of Case 2 with fixed α classified by the largest magnitudes in sub-catalogs (ETAS parameter results of Case 1 are plotted without numbering for comparison).

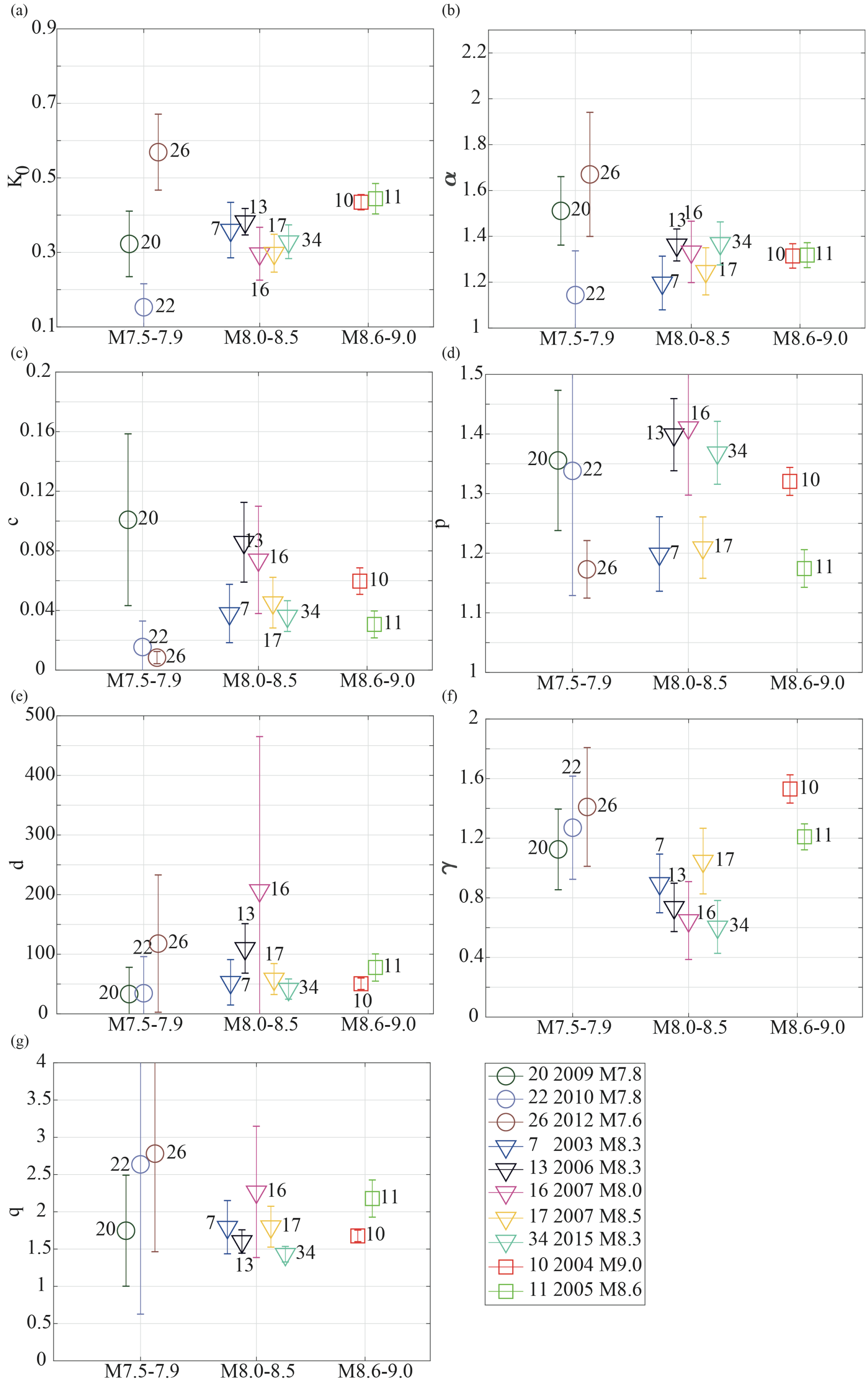

Figure 5. ETAS parameter results classified by mainshock magnitudes for Case 3 based on individual sequences.

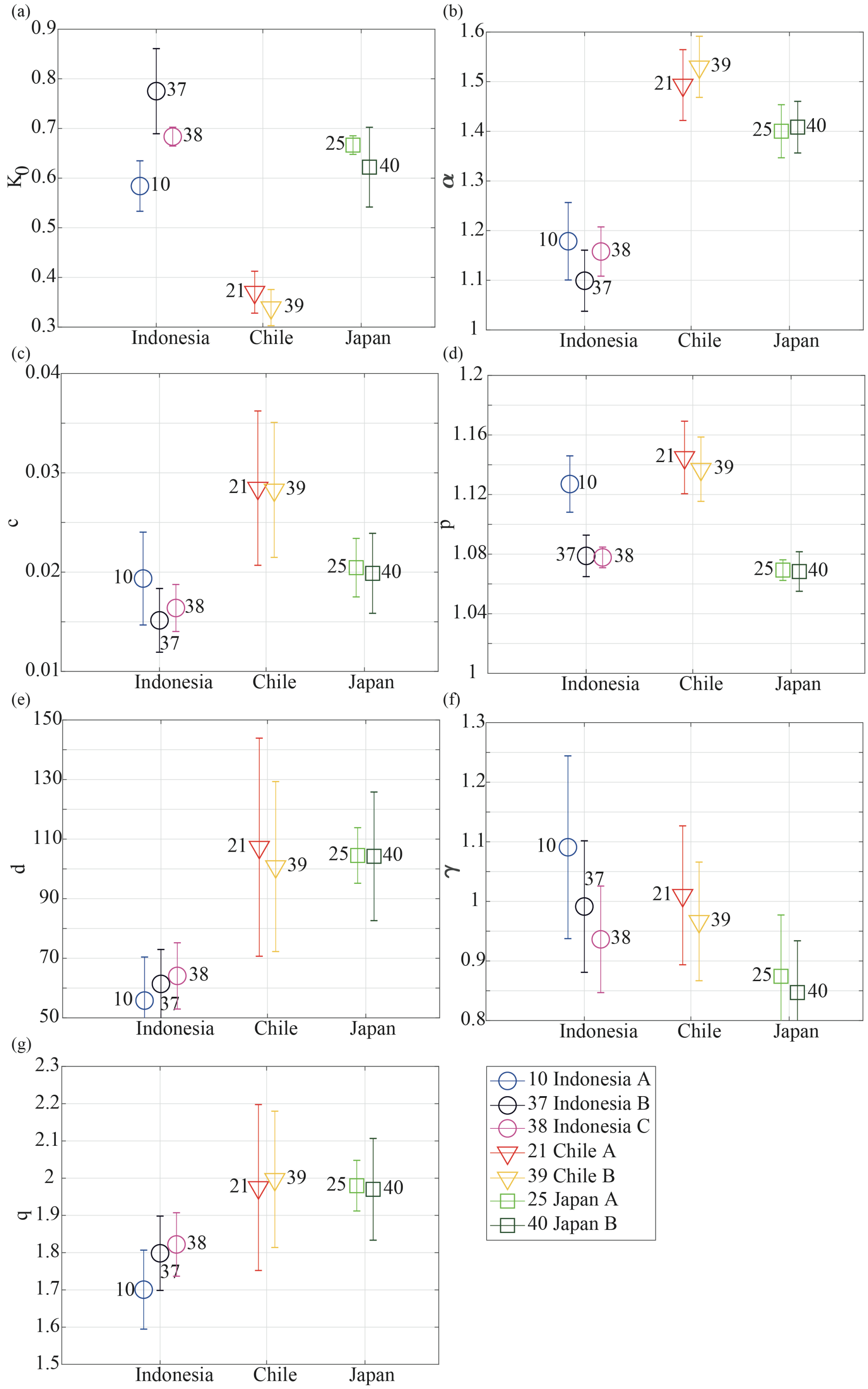

Figure 6. Parameter results from the sub-catalogs with multiple subduction earthquakes in Indonesia, Chile, and Japan.

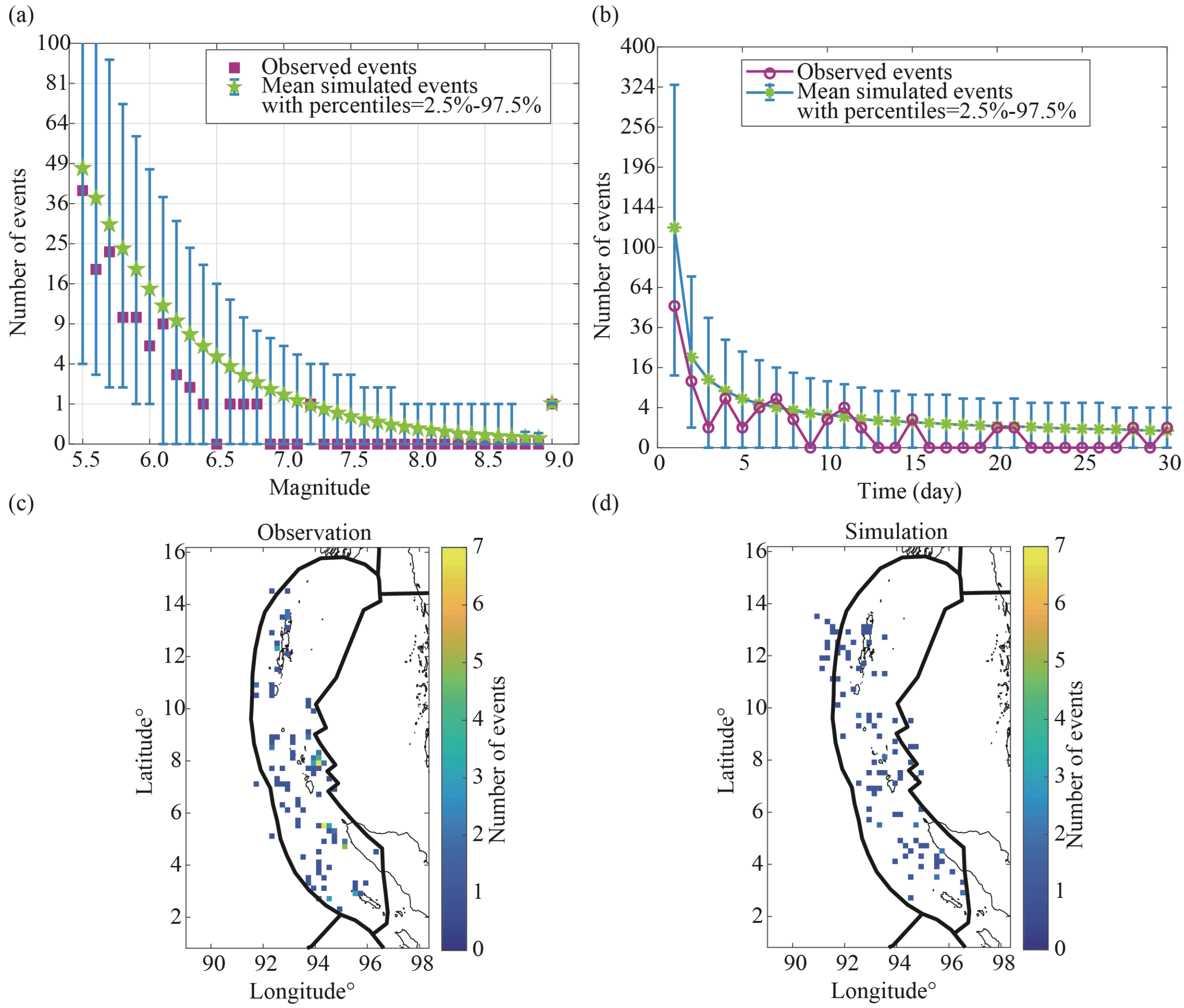

Figure 7. Comparison of observed and simulated M5.5+ aftershocks of the 2004 Aceh-Andaman earthquake: (a) magnitude frequency distribution in square root scale during the first three months, (b) daily number of events during the first 30 days, (c) observed 2D aftershock histograms during the first three months, (d) a simulated 2D aftershock histogram over the same period.

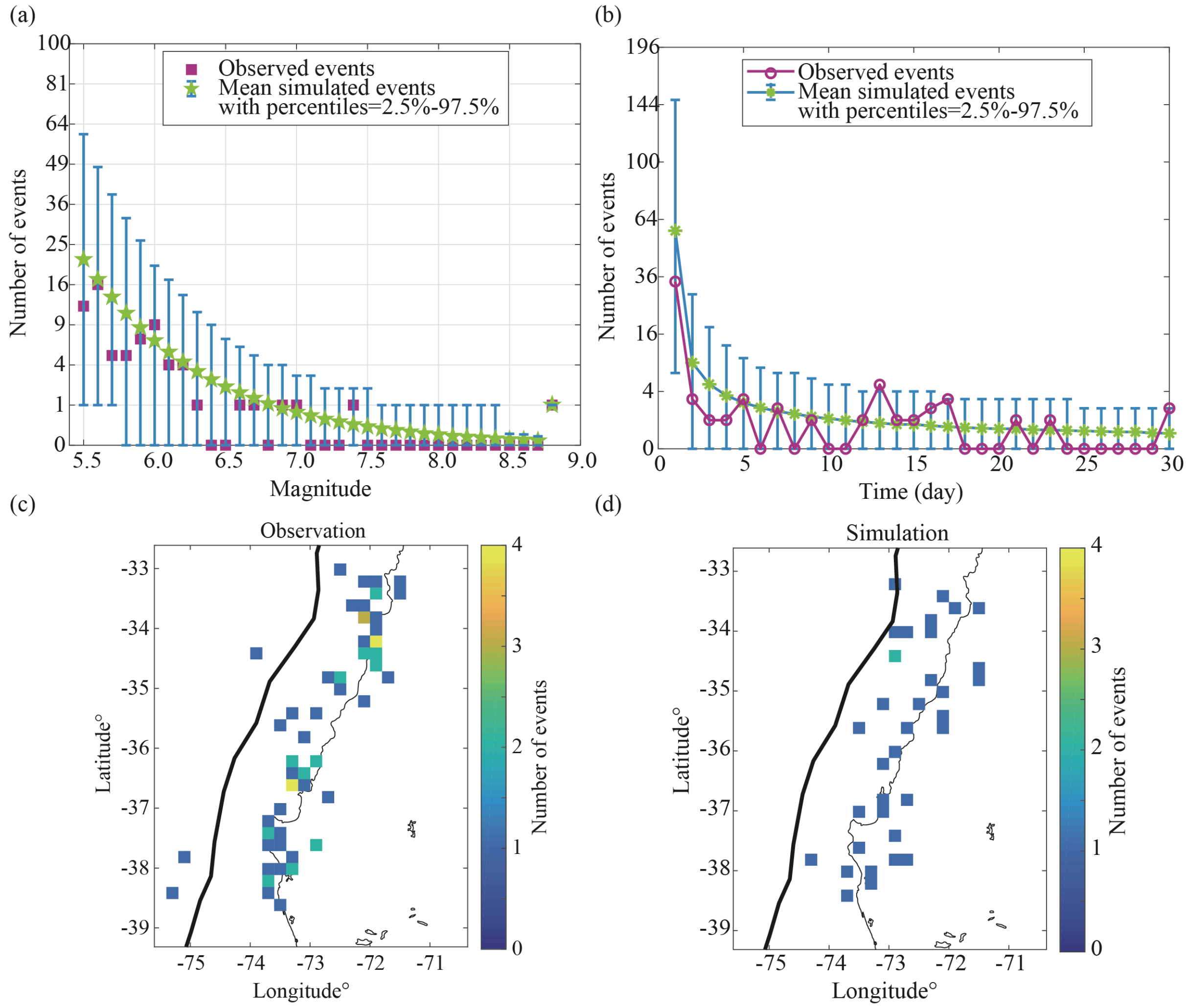

Figure 8. Comparison of observed and simulated M5.5+ aftershocks after the 2010 Maule earthquake: (a) magnitude frequency distribution during the first three months, (b) daily number of events during the first 30 days, (c) observed 2D aftershock histogram during the first three months, (d) a simulated 2D aftershock histogram over the same period.

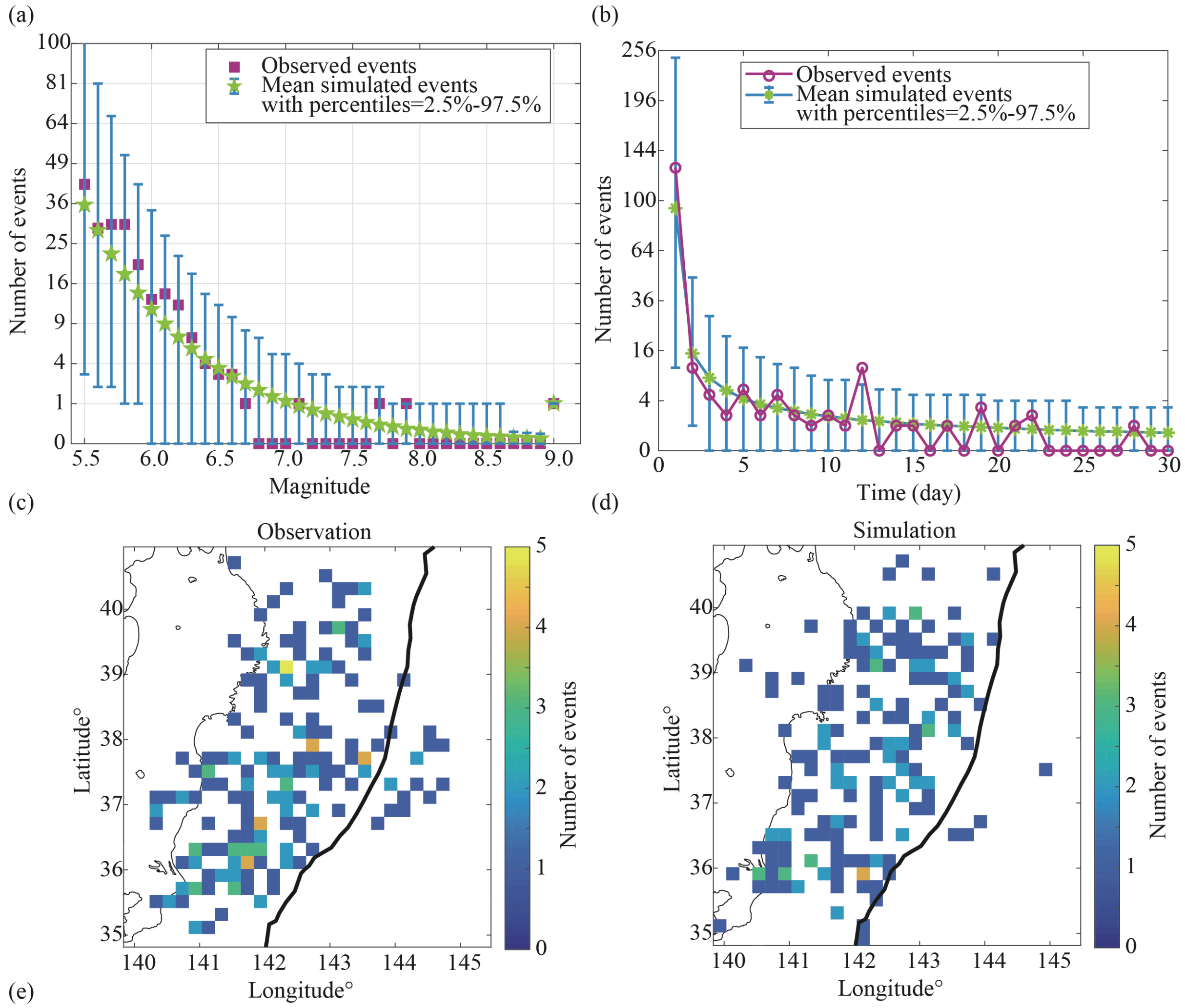

(e)

Figure 9. Comparison of observed and simulated M5.5+ aftershocks after the 2011 Tohoku earthquake: (a) magnitude frequency distribution in square root scale during the first three months, (b) daily number of events during the first 30 days, (c) observed 2D aftershock histogram during the first three months, (d) a simulated 2D aftershock histogram during the first three months.

Appendix A

Comparison of the Mainshock Rupture Model and the Scaling Law

The purpose of **Appendix A** is to compare the scaling law of Thingbaijam *et al.* (2017) with the estimated rupture lengths and widths of the global megathrust events in **Table 2**, as we will apply the scaling law in the ETAS simulation framework to simulate the anisotropic mainshock rupture dimensions (and their variability). Most M≥8 earthquakes agree well with the scaling laws, but there are small discrepancies. For example, 10 of 13 M≥8 events are in the range of one standard deviation of the rupture area scaling law in **Figure A1**(c). However, 14 out of 23 events with **M**7.5-7.9 fall outside the mean plus/minus one standard deviation range, showing a larger fluctuation than **M**8.0-**M**9.0 events. This suggests the standard deviation of the scaling law is smaller than the observed variability of **M**7.5-7.9 events. In addition, the rupture areas of Events 23, 26, and 28 (orange circles in **Figure A1**(c)) are smaller than expected. This may be because the fault type of these events has a strike-slip component (oblique reverse) and the scaling law for strike-slip events predicts smaller areas than for subduction-interface events (Thingbaijam *et al.*, 2017). Because the bulk of the **M**8.0-**M**9.0 earthquakes agree with the scaling laws, however, we conclude that the laws are appropriated for the purpose of simulating anisotropic mainshock ruptures.

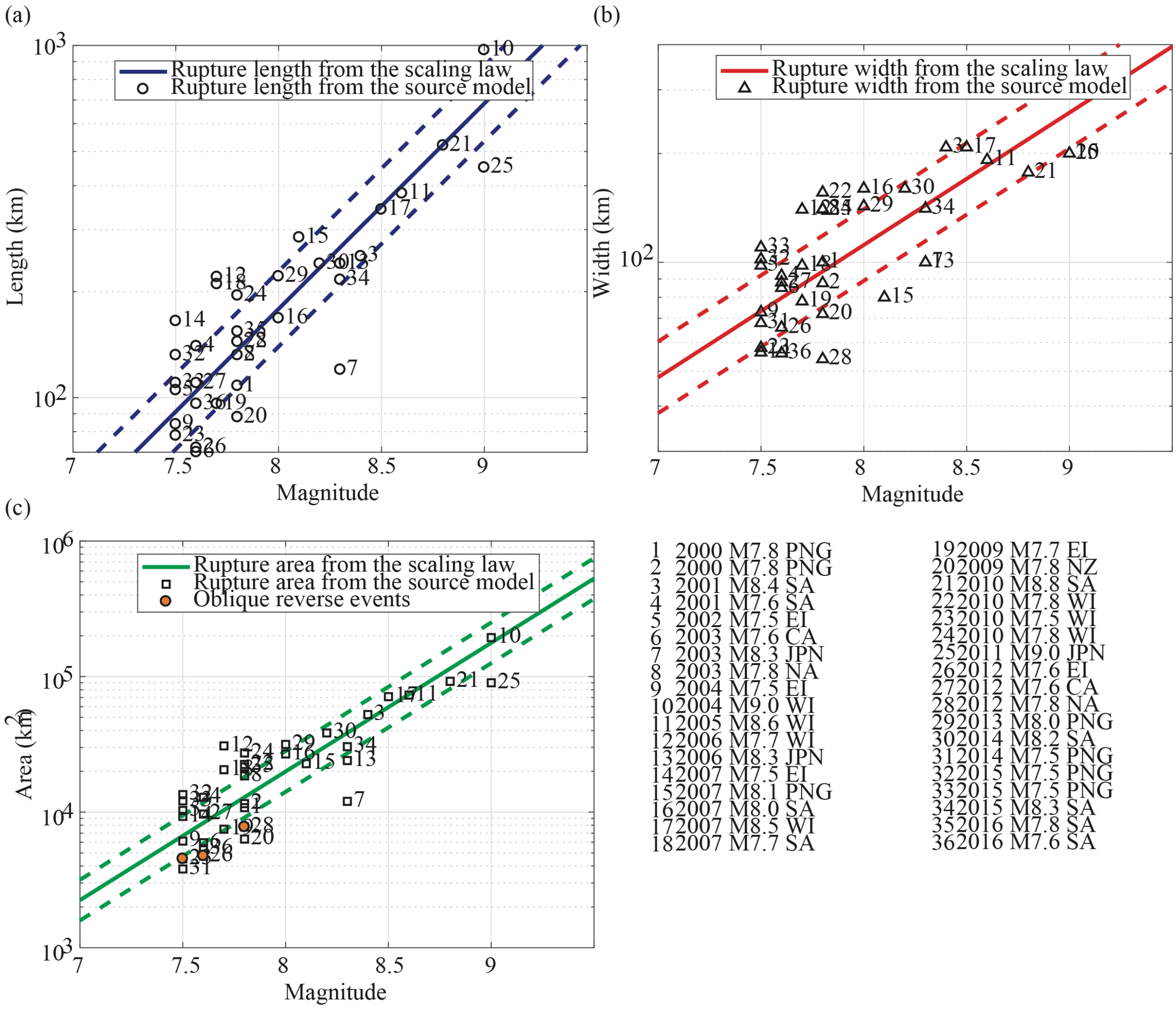

Figure A1. Comparisons between empirical scaling laws (Thingbaijam et al., 2017) and effective rupture models of megathrust M≥7.5 earthquakes: (a) rupture length, (b) rupture width, and (c) rupture area. Japan (JPN), Eastern Indonesia (EI), Papua New Guinea (PNG), Western Indonesia (WI), North America (NA), Central America (CA), and South America (SA).

Appendix B

Boxplots of the ETAS parameters for Case 1

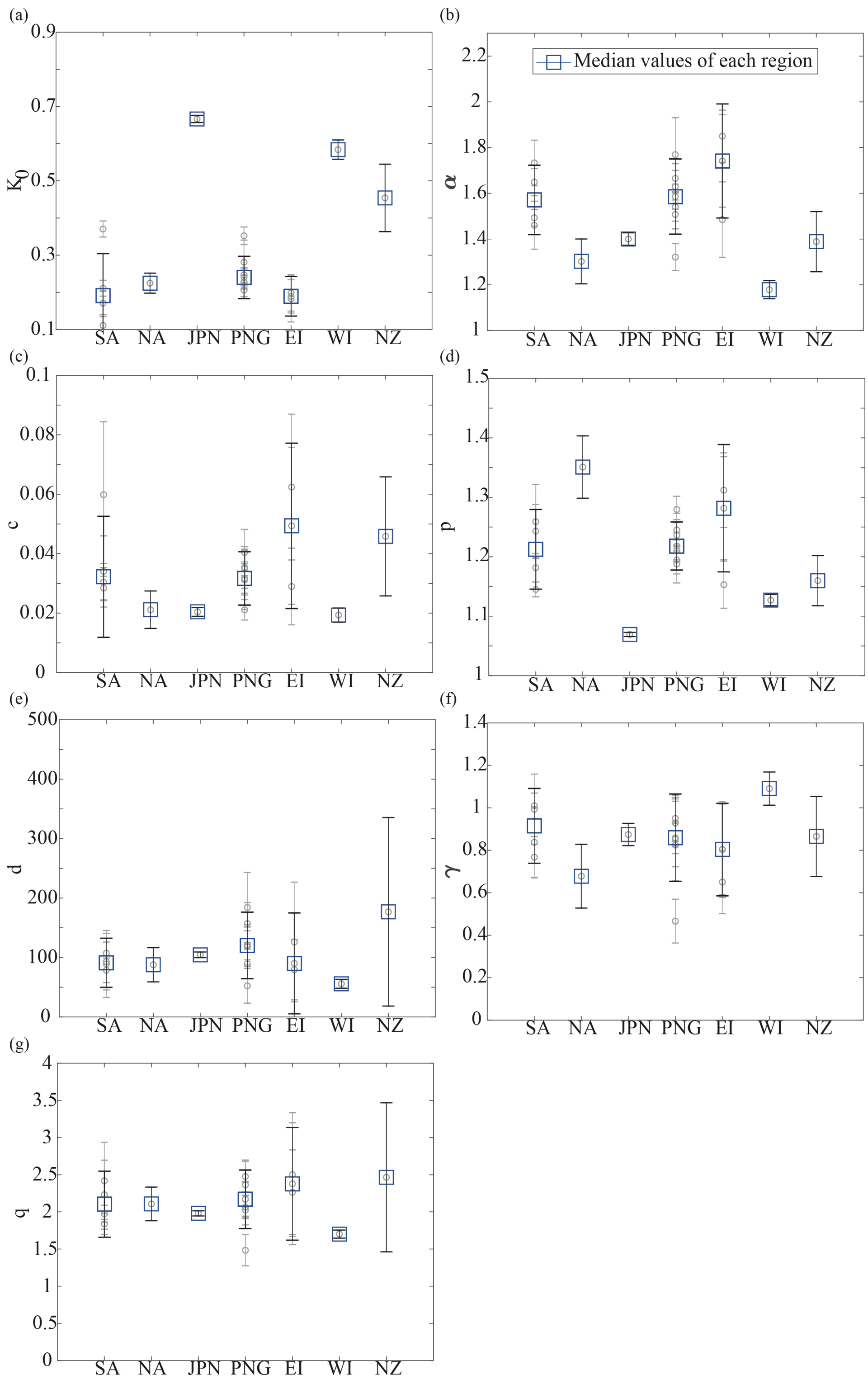

Figure B1. Boxplots of the ETAS parameter estimates classified by region in South America (SA), North America (NA), Japan (JPN), Papua New Guinea (PNG), Eastern Indonesia (EI), western Indonesia (WI), and New Zealand (NZ) for Case 1 based on long-time catalogs with all ETAS parameters free. Individual samples are plotted in circles with error bars.

Standard errors of ETAS parameters for each geographical region from boxplots

The total stand error (SE_{total}) of ETAS parameters for each geographical region is calculated by:

$$\mathrm{SE_{total}} = \sqrt[2]{(\mathrm{SE_{mean}})^2 + (\mathrm{SE_{individual}})^2} \quad \text{(B1)}$$

where SE_{mean} is the standard deviation of the estimated ETAS parameters in each geographical region and $SE_{individual}$ is the square root of the mean of all variances in each region.

1060 ***ETAS parameters classified by the largest magnitude in each sub-catalog for Case 1***

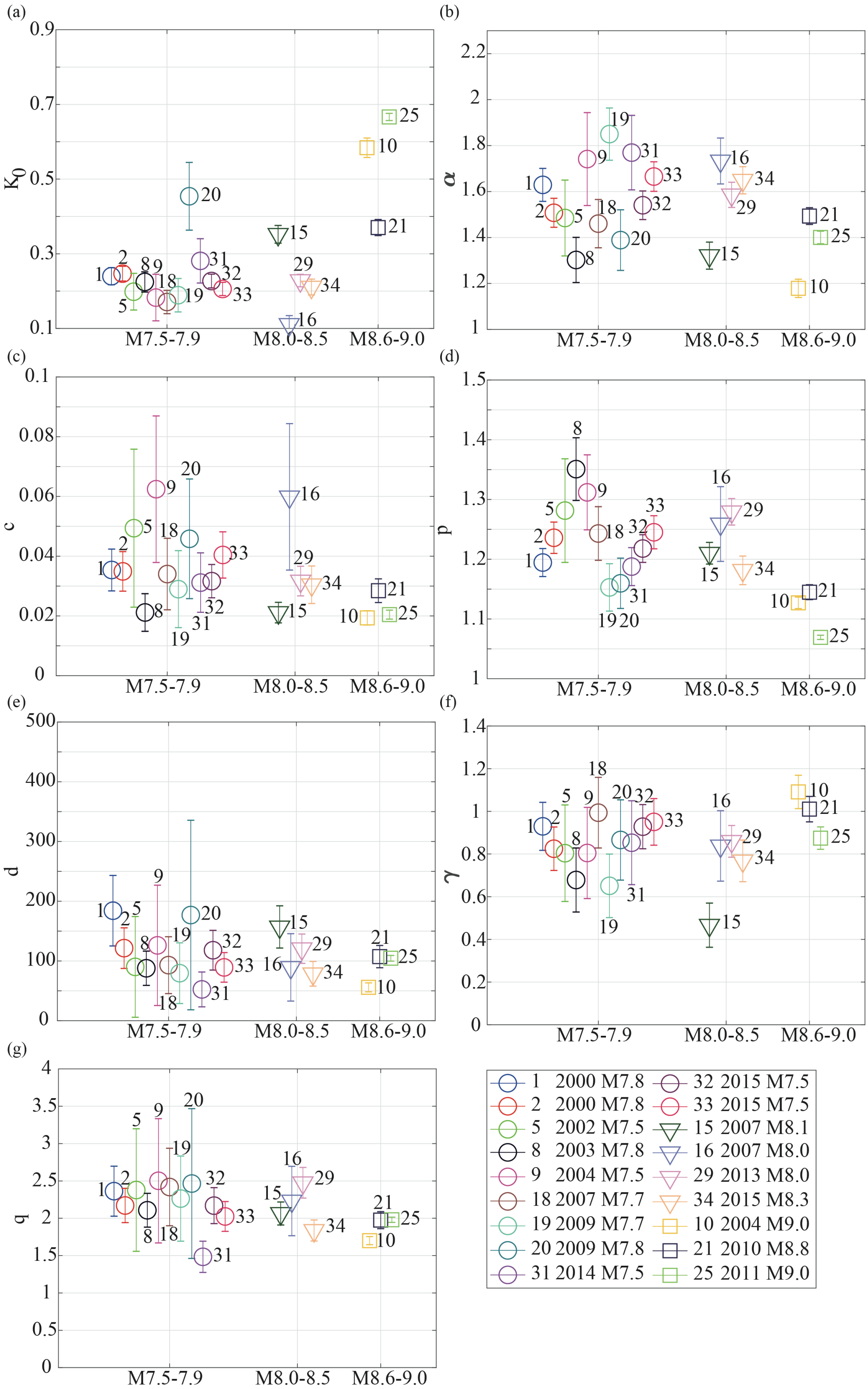

1061

Figure B2. ETAS parameter results classified by the largest magnitude for Case 1 based on long time period catalogs with all ETAS parameters free.

ETAS parameters classified by region for Case 2

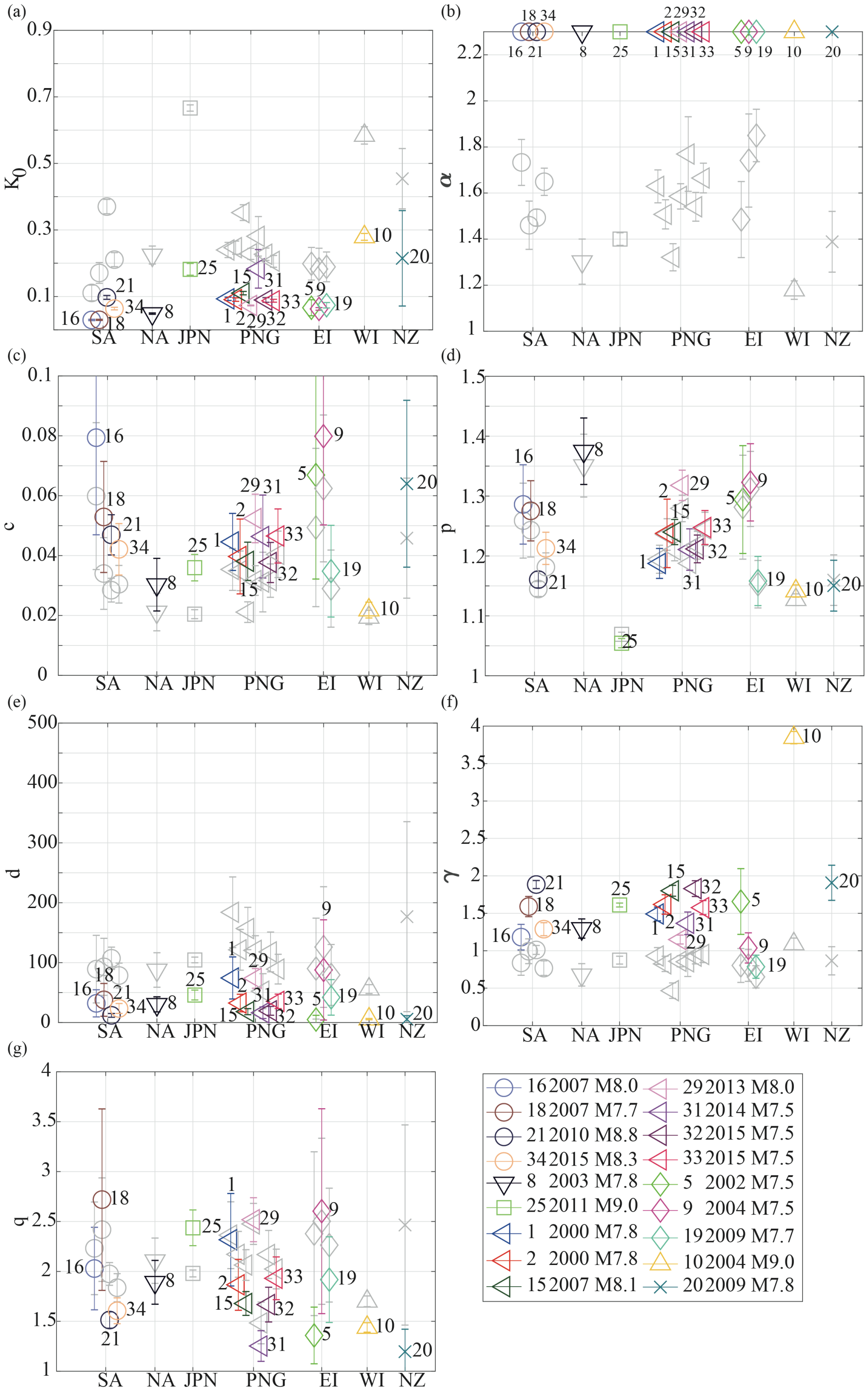

Figure B3. ETAS parameter results classified by region in South America (SA), North America (NA), Japan (JPN), Papua New Guinea (PNG), Eastern Indonesia (EI), Western

Indonesia (WI), and New Zealand (NZ) for Case 2 based on long time period catalogs with fixed α.

Boxplots of the ETAS parameters for Case 2

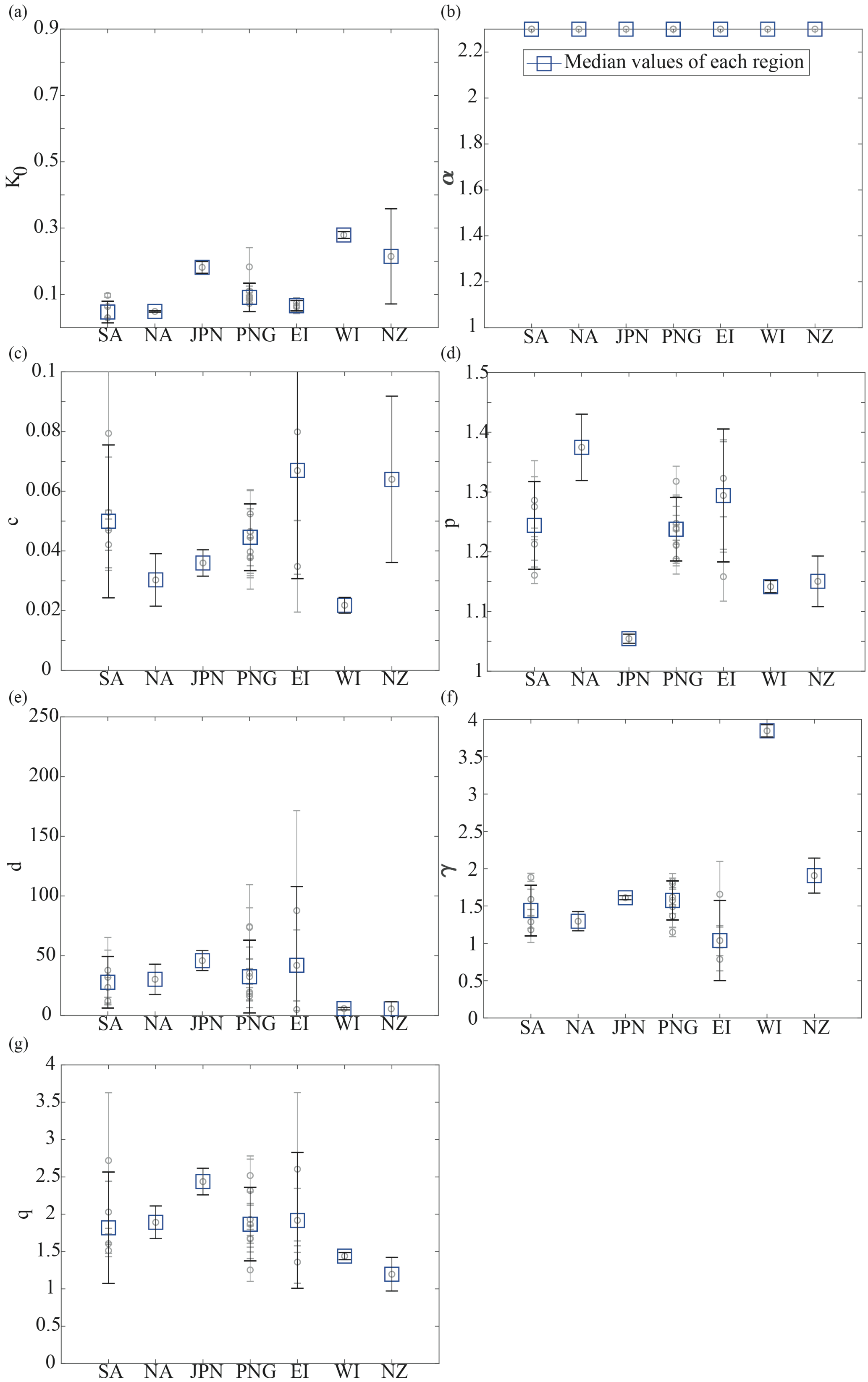

Figure B4. Boxplots of the ETAS parameter estimates classified by region in South America (SA), North America (NA), Japan (JPN), Papua New Guinea (PNG), Eastern Indonesia (EI), western Indonesia (WI), and New Zealand (NZ) for Case 2 based on long time period catalogs with fixed α. Individual samples are plotted in circles with error bars.

Table B1. Summary of the p_{lm} values of ETAS parameters for Case 3 (Boldface indicates significant co-dependence).

	K_0	α	c	p	d	γ	q
Magnitude	1.0000	0.8345	1.0000	1.0000	1.0000	1.0000	0.2750
Rupture length	1.0000	0.8494	1.0000	1.0000	1.0000	1.0000	1.0000
Rupture width	1.0000	0.1558	1.0000	1.0000	1.0000	1.0000	1.0000
Rupture area	1.0000	0.4532	1.0000	1.0000	1.0000	1.0000	1.0000